A Stalagmite Test of North Atlantic SST and Iberian Hydroclimate Linkages over the Last Two Glacial Cycles

Rhawn F. Denniston[a*], Amanda N. Houts[a1], Yemane Asmerom[b], Alan D. Wanamaker, Jr.[c], Jonathon A. Haws[d], Victor J. Polyak[b], Diana L. Thatcher[c], Setsen Altan-Ochir[a], Alyssa C. Borowske[a2], Sebastian F.M. Breitenbach[e], Caroline C. Ummenhofer[f], Frederico T. Regala[g], Michael M. Benedetti[h], Nuno Bicho[i]

[a] Department of Geology, Cornell College, Mount Vernon, Iowa 52314 USA
[b] Department of Earth and Planetary Sciences, University of New Mexico, Albuquerque, New Mexico 87131 USA
[c] Department of Geological and Atmospheric Sciences, Iowa State University, Ames, Iowa 50011 USA
[d] Department of Anthropology, Louisville University, Louisville, Kentucky 40208 USA
[e] Institute for Geology, Mineralogy, and Geophysics, Ruhr-University Bochum 44801 Germany
[f] Department of Physical Oceanography, Woods Hole Oceanographic Institution, Woods Hole, Massachusetts 02543 USA
[g] Associação de Estudos Subterrâneos e Defesa do Ambiente, Torres Vedras, Portugal
[h] Department of Geography and Geology, University of North Carolina Wilmington, Wilmington, North Carolina 28403 USA
[i] Center for Archaeology and Evolution of Human Behaviour, Universidade do Algarve, Faro, Portugal

[*] corresponding author

[1] current address: Department of Earth Sciences, University of New Hampshire, Durham, New Hampshire 03824 USA

[2] current address: Department of Ecology and Evolutionary Biology, University of Connecticut, Storrs, Connecticut 06269 USA

Keywords

Iberia, hydroclimate, stalagmite, oxygen isotope, carbon isotope, $\delta^{234}U$, pollen, sea surface temperature

Abstract

Close coupling of Iberian hydroclimate and North Atlantic sea surface temperature (SST) during recent glacial periods has been identified through the analysis of marine sediment and pollen grains co-deposited on the Portuguese continental margin. While offering precisely correlatable records, these time series have lacked a directly-dated, site-specific record of continental Iberian climate spanning multiple glacial cycles as a point of comparison. Here we present a high-resolution, multi-proxy (growth dynamics and δ^{13}C, δ^{18}O, and δ^{234}U values) stalagmite-based, composite record of hydroclimate from two caves in western Portugal across the majority of the last two glacial cycles (~230 ka). At orbital and millennial scales, stalagmite-based proxies for hydroclimate proxies covaried with SST, with elevated δ^{13}C, δ^{18}O, and δ^{234}U values and/or growth hiatuses indicating reduced effective moisture coincident with periods of lowered SST during major ice-rafted debris events, in agreement with changes in palynological reconstructions of continental climate. While in many cases the Portuguese stalagmite record can be scaled to SST, in some intervals the magnitudes of stalagmite isotopic shifts, and possibly hydroclimate, appear to have been decoupled from SST.

1. Introduction

The Portuguese continental margin is an important location for understanding variations in paleoceanographic conditions over orbital and millennial-scales (Hodell et al., 2013; Voelker and de Abreu, 2011). Here, marine sediments record basin-wide oceanographic signals while co-deposited pollen grains track coeval vegetation changes occurring across Iberia. Integrated analysis of these proxies has revealed a close coupling of North Atlantic SST, regional climate, and Iberian ecosystems during the last three glacial cycles, including changes in vegetation dynamics (Sánchez Goñi et al., 2002; Tzedakis et al., 2004; Roucoux et al., 2006; Martrat et al., 2007; Naugthon et al., 2007; Sánchez Goñi et al., 2008), atmospheric circulation (Sánchez Goñi et al., 2013), and fire frequency (Daniau et al., 2007). One commonly applied palynological metric is the abundance of temperate tree pollen, which rises during warm and wet conditions associated both with interglacials and Greenland interstadials, concomitant with shifts in Iberian margin SST (Sánchez Goñi et al., 2002; Tzedakis et al., 2004; Combourieu-Nebout et al., 2009; Fletcher et al., 2010; Chabaud et al., 2014). However, the nature of such land-sea connections is partially obscured by the size of catchments from which the pollen are derived, with some

66   reaching into central Iberia and spanning a range of environmental settings subject to varying

67   climatic influences (Martin-Vide and Lopez-Bustins, 2006; Naughton et al., 2007) (Fig. 1).

68   Testing the links between terrestrial and marine systems benefits from continental climate

69   archives that provide precisely-dated and high resolution rainfall-sensitive time series spanning

70   tens of millennia, but such records remain rare in Iberia, particularly near the west Iberian

71   margin (Fletcher et al., 2010; Moreno et al., 2012; Stoll et al., 2013). Here we present a

72   composite stalagmite record of four proxies for hydroclimate – growth dynamics and δ^{13}C, δ^{18}O,

73   and δ^{234}U values – spanning the majority of the last and penultimate glacial cycles (~230 ka) at

74   two cave sites in western Portugal. These time series offers a rare, site-specific continental record

75   capable of examining the coherence of SST controls on Iberian climate and ecosystem dynamics

76   across glacial and interglacial periods. The new record provides a continental perspective of

77   hydroclimate dynamics linked to regional oceanographic conditions.

78

79   **2. Samples and Regional Setting**

80   *2.1 Environmental Setting*

81   We report the analysis of five stalagmites (BG41, BG66, BG67, BG611, BG6LR) from

82   Buraca Gloriosa (BG; 39º32'N, 08º47'W; 420 m a.s.l.) and one stalagmite (GCL6) from Gruta

83   do Casal da Lebre (GCL; 39˚18'N, 9˚16'W; 130 m a.s.l.), two caves in western Portugal (Fig. 1).

84   Environmental conditions in BG and GCL are well suited for speleothem paleoclimate

85   reconstruction (see below). BG and GCL are located within the Meso-Mediterranean bioclimatic

86   zone that dominates much of Iberia (Fig. 1). This region is characterized by strong seasonality,

87   with warm, dry summers and cool, wet winters (Fig. 2) associated with the winter westerlies

88   (Blanco Castro et al., 1997). In contrast, the Atlantic zone, north of the Douro River, is cooler,

89   wetter, and less strongly seasonal. In the Pleistocene, the transition between these zones likely

90   shifted southward with Mediterranean-type vegetation restricted to refugia (Rey Benayas and

91   Scheiner, 2002).

92   Over interannual scales, the hydroclimate of Iberia is tightly coupled with the winter

93   North Atlantic Oscillation (NAO) (Fig. 3), an atmospheric dipole that strongly influences

94   precipitation across much of western Europe and that more broadly reflects the strength and

95   positioning of the Azores high pressure system, which steers storm tracks contained within the

96   westerlies into or north of Iberia (e.g., Trigo et al, 2002; Paredes et al., 2006; Trouet et al., 2009;

97 Cortesi et al., 2014). The NAO is typically measured as the NAO index, which is calculated

98 using atmospheric pressure differences between Iceland and Lisbon (or the Azores) (Barnston

99 and Livezey, 1987). The nature of the influence of the NAO varies across Iberia, but it is

100 strongly correlated to rainfall in western Portugal (Fig. 3), with a positive NAO index associated

101 with a steeper pressure gradient and elevated Iberian aridity. Iberian precipitation has also been

102 linked closely to SST in regions ranging from the western North Atlantic to the Iberian margin

103 (Lorenzo et al., 2010) where ocean circulation is dominated by the southward-flowing Portugal

104 Current and the near-coastal and north-flowing Iberian Poleward Current, two systems that

105 transport pollen from river mouths along the continental shelf (Fig. 1).

106

107 *2.2 Cave Settings*

108 Buraca Gloriosa cave is located near the town of Alvados, 30 km from the Atlantic

109 Ocean, and within middle Jurassic limestones of the Estremadura Limestone Massif (Rodrigues

110 and Fonseca, 2010), a topographically distinct region in central Portugal (Fig. 1). The ~35 m-

111 long cave is accessed through a single, small (~0.5 m^2) entrance at the top of a collapse at the

112 base of a 30 m-high escarpment (Fig. 4). The cave is well decorated although little active growth

113 is occurring today. Vegetation above the cave is primarily shrubs, small trees, and mosses,

114 hosted by a thin (< 10 cm) and highly organic soil layer.

115 Gruta do Casal da Lebre is located ~5 km from the coastal town of Peniche in upper

116 Jurassic limestones. The cave is 130 m long and contains a single, one m^2 entrance that opens

117 onto a 7 m vertical shaft (Fig. 4). This entrance has been closed with a solid metal door in recent

118 decades in order limit access to the cave, and this modification likely has reduced air exchange in

119 the GCL relative to its original state. Like BG, GCL hosts little active calcite deposition, but

120 contains numerous fossil stalagmites and stalactites. The vegetation over the cave has been

121 replaced in recent decades by stands of eucalyptus that grow in thin (<1-5 cm), clay-rich soils.

122

123 *2.3 Pollen Sources*

124 Pollen deposited on the west Iberian margin are sourced primarily from vegetation

125 inhabiting the watersheds of the major west-flowing stream systems draining Portugal and Spain,

126 which are (from north to south) the Douro, Tagus, and Sado rivers. The areas encompassed by

127 these streams are large (79,000, 81,000, and 7,650 km^2, respectively) and span a variety of

128 elevations. The Tagus and Sado are primarily responsible for pollen deposited southwest of
129 Portugal, while the Douro plays an important role in delivering pollen to the more northwesterly
130 sites (Fig. 1). Prevailing wind patterns likely prevent substantial transport of pollen from Iberia
131 to the western Portuguese margin (Naughton et al., 2007). The pollen data presented here were
132 measured in three closely spaced cores from the southwest Iberian margin (MD01-2443: 250-194
133 ka (Roucoux et al, 2006; Tzedakis et al., 2004); MD01-2444: 193-136 ka (Margari et al., 2010;
134 Margari et al., 2014); MD95-2042: 141-1 ka (Sánchez Goñi et al., 2008; Sánchez Goñi et al.,
135 2013) (Fig. 1) and are integrated here into a single time series.
136

137 **3. Materials and Methods**
138 *3.1 Environmental Monitoring*
139   Environmental conditions were measured at both cave sites over a multi-year period, with
140 data measured in two-hour intervals near the areas where the stalagmites were deposited.
141 Temperature and relative humidity were obtained using HOBO U23 automated sensors while
142 barometric pressure was recorded with HOBO U20L loggers. Drip rates were monitored at BG
143 with Stalagmate acoustic drip counters (Collister and Mattey, 2008), which were installed at the
144 rear of the cave.
145

146 *3.2 Uranium-Series Dating*
147   Stalagmite chronologies were constructed with a total of 72 ^{230}Th dates obtained at the
148 University of New Mexico (Table 1) using the methods of Asmerom et al. (2010). For dating of
149 stalagmite carbonate, powders ranging from 100-200 mg were transferred into 30 ml Teflon
150 beakers, weighed, dissolved in 15N nitric acid, and then spiked with a mixed ^{229}Th-^{233}U-^{236}U
151 tracer and processed using column chemistry methods. U and Th fractions were dissolved in 5 ml
152 of 3% nitric acid and transferred to analysis tubes for measurement on a Thermo Neptune MC-
153 ICP-MS. U and Th isotopic ratios were aspirated into the Neptune using a Cetac Aridus II low
154 flow desolvating nebulizer and run as static routines. All isotopes of interest were measured in
155 Faraday cups, except for ^{234}U and ^{230}Th, which were measured in the secondary electron
156 multiplier (SEM). Gains between the SEM and the Faraday cups were determined using standard
157 solutions of NBL-112 for U and an in-house ^{230}Th-^{229}Th standard for Th that was measured after

158   every fifth sample; chemistry blanks reveal U and Th blanks below 20 pg. Ages are reported

159   using two standard deviation errors and are relative to the year AD 1950.

160   For BG stalagmites, corrections were made for unsupported ^{230}Th using a ^{230}Th/^{232}Th

161   ratio of 13.5 ppm (±50%), a value determined from isotopic analysis of cave dripwater. To

162   obtain this vaue, 108 ml of dripwater were transferred into six 30 ml Teflon beakers. These

163   beakers were fluxed in 6N HCl for an hour, rinsed, and heated gently on a hotplate until

164   approximately 1-2 ml of fluid remained in each. All solutions were then combined into a single

165   30 ml Teflon beaker, spiked with the same tracer described above (which contains HF), fluxed,

166   and then taken to complete dryness. The resulting precipitate was dissolved with 15N HNO3,

167   dried down, and dissolved again in 7N nitric acid, and processed with the same column

168   chemistry methods used for the stalagmite samples. We lack independent constraints on the

169   initial Th ratio for the GCL stalagmite, and thus apply the default value of 4.4 ppm (±50%). This

170   difference in the initial Th ratio impacts the corrected ages of GCL6 by 0.5-3.0 kyr, and thus

171   does not meaningfully impact our interpretations.

172   Age models were developed via multiple polynomial interpolations between dated

173   intervals using the COPRA age modeling software (Breitenbach et al., 2012) (Fig. 5). Aside from

174   providing age models, COPRA also yields mean modeled stable isotope values and confidence

175   intervals (Supp. Fig. S1 and S2). Here we rely primarily here on the original δ^{18}O and δ^{13}C

176   values because COPRA-derived median values reflect statistically robust variations, but reduce

177   to some degree the range of isotopic variability. For COPRA, a dummy age was included in the

178   age model for BG41 in order to extrapolate below the hiatus, which is only possible with at least

179   two dated points. The value of this dummy age was based on the assumption that it maintains a

180   stratigraphically correct slope (i.e. higher sections of the stalagmite represent younger material).

181   The dummy age was applied a conservative error, meaning that it was as large as possible

182   without causing stratigraphic inversion with respect to the bounding ages.

183

184   *3.3 Stable Isotope Ratios*

185   A total of 1,510 stable isotope analyses were performed on calcite samples milled from

186   the central axis of each stalagmite. After milling, powders were weighed (~200 μg) and

187   transferred to reaction vessels that were flushed with ultra-pure helium. Samples were then

188   digested using >100% H$_3$PO$_4$ and equilibrated overnight (~16 hours) at 34˚C before being

189   analyzed. Isotopic ratios were measured using a GasBench II with a CombiPal autosampler

190   coupled to a Thermo Finnigan Delta Plus XL mass spectrometer at Iowa State University. A

191   combination of internal and external standards was run after every fifth sample, as well as before

192   and after each batch, in order to ensure reproducibility. Oxygen and carbon isotope ratios are

193   presented in parts per mil (‰) relative to the Vienna Pee Dee Belemnite carbonate standard

194   (VPDB). Average precision for both $\delta^{13}C$ and $\delta^{18}O$ analyses is better than ±0.1‰ (1σ).

195   For isotopic analyses of soil organic matter and vegetation collected from above the

196   caves, samples were dried, crushed, and transferred to tin boats. Carbon isotopic ratios were

197   measured using a Thermo Finnegan Delta Plus XL mass spectrometer in continuous flow mode

198   coupled with a Costech Elemental Analyzer. Caffeine (IAEA-600), cellulose (IAEA-CH-3), and

199   acetanilide (laboratory standard) isotopic standards yielded an average analytical uncertainty for

200   carbon of ±0.09‰ 1σ (VPDB). Dripwater samples were measured using a Picarro L2130-i

201   Isotopic Liquid Water Analyzer, with autosampler and ChemCorrect software. Each sample was

202   measured six times, with only the last three injections used to determine isotopic values in order

203   to minimize memory effects. Three reference standards (VSMOW, IAEA-OH-2, IAEA-OH-3)

204   were used for regression-based isotopic corrections and to assign the data to the appropriate

205   isotopic scale. Reference standards were measured at least once every five samples. The average

206   analytical uncertainty for $\delta^{18}O$ measurements was ± 0.1‰ 1σ (VSMOW).

207

208   *3.4 Stalagmite Mineralogy and Fabrics*

209   The calcite comprising the BG samples ranges across a variety of fabrics including a

210   faster-growing, white, fibrous form and slower-growing, dense, clear structure (Fig. 6; Supp. Fig.

211   S3). In some areas of two samples - BG6LR and BG67 - sharp changes between the two forms

212   within the same growth horizons mark intervals of recrystallization. BG6LR, which grew

213   discontinuously over much of the last glacial cycle, suffered from alteration of early and middle

214   Holocene material, which was therefore excluded from this analysis. BG67 is characterized

215   primarily by fibrous calcite that has been recrystallized to clear, dense calcite in a narrow band

216   descending through its core. U/Th dates from the fibrous calcite on the margins of the growth

217   surface reveal open system behavior and thus this portion of BG67 was excluded from

218   discussion. A small amount of recrystallization is evident in portions of GCL6 but the

219   consistency of U/Th dates, and the trends in stable isotopes suggest that this sample retains

220   reliable paleoclimatic information. Growth position changed at numerous times in several of

221   these stalagmites, and our sampling strategy accounted for these changes so as to consistently

222   collect samples for stable isotopic analysis from the top surface (cap) of each stalagmite rather

223   than the margins.

224

225   **4. Results**

226   *4.1 Environmental Monitoring*

227   Temperature and relative humidity collected inside both caves document environmental

228   conditions over a four-year period. Relative humidity remained stable at ~100% in both caves.

229   Temperatures, while different at the two sites, exhibited similar seasonal variability that

230   approximates the mean average temperature of the region (14.2±0.4˚C at BG and 16.2±0.3˚C at

231   GCL for August 2012-January 2018) (Fig. 7).

232   Dripwater was collected at BG both over the course of minutes during site visits on four

233   separate occasions (November 2014, October 2015, March 2016, January 2018) and as months-

234   long integrated samples. A total of 25 dripwater samples were analyzed for stable isotopic

235   values. Dripwater $\delta^{18}O$ values range from -2.4‰ to -4.6‰, with a mean of -3.8±0.8‰ (Supp

236   Table 1), although as the timing of site visits varied, this value clearly is impacted by seasonal

237   controls on precipitation (and thus infiltration) oxygen isotope values. Drip rates were measured

238   for much of the period spanning June 2014 to January 2018 (for a total of ~36 months) and

239   exhibit seasonal variations tied to the winter wet and summer dry seasons, as well as individual

240   rain events (Fig. 7).

241

242   *4.2 U-Th Dates and Age Models*

243   ^{234}U-^{230}Th dating of BG and GCL stalagmites reveals growth across approximately three

244   quarters of the last 230 ka, with periods of deposition interrupted by numerous hiatuses of

245   varying length, with the longest gaps from 160-147, 97-87, 72-60, 41-36, 32-30, and 17-15 ka

246   (Fig. 5 and 6). These features, coupled with repeated changes in growth direction, complicate

247   construction of a chronology in some intervals. Macroscopic petrographic discontinuities suggest

248   the presence of several short-lived hiatuses, but these were included as gaps in the age models

249   only where U/Th dates reveal an identifiable temporal offset. For example, the marine isotope

250   stage (MIS) 6/5e boundary recorded by stalagmite BG67 is marked by both a change in drip

251 position and a sharp transition from dense, clear calcite to a white, fibrous form. Taken together,

252 it is clear that a hiatus of some duration occurred at this time. However, these isotope data are

253 presented as being uninterrupted given the continuity of $\delta^{18}O$ values and no U/Th evidence for a

254 long-lived hiatus (Fig. 6).

255

256 *4.3 Assessing Environmental Signals in Speleothem Isotopic Ratios*

257 We used two approaches to assess the fidelity of BG/GCL carbon and oxygen isotopes as

258 records of past environmental variability. First, Hendy Tests, in which stalagmite isotopic ratios

259 must satisfy two criteria in order to be considered as having crystallized near isotopic

260 equilibrium with cave dripwater (Hendy, 1971), were performed for each stalagmite. The first

261 half of the Hendy Test involves analysis of multiple isotopic analyses performed on samples

262 drilled at increasing distance from the central growth axis along the same series of growth layers.

263 The conceptual justification for this approach is that dripwater, and thus calcite, $\delta^{18}O$ values

264 should remain constant down the stalagmite flanks because ^{16}O preferentially lost to CO_2 out-

265 gassing is replenished by CO_2 hydration and hydroxylation reactions. Progressive ^{18}O

266 enrichment associated with kinetic effects tied to Rayleigh distillation suggests isotopic

267 disequilibrium. No such consistent trends toward elevated oxygen isotopic ratios are found (Fig.

268 8), and thus the BG/GCL stalagmites appear to satisfy the first criterion of the Hendy Test.

269 The second portion of the Hendy Test is based on the degree of covariation of carbon and

270 oxygen isotopic ratios. Oxygen isotopic ratios of speleothem calcite reflect those of infiltrating

271 fluids, which are generally close to the $\delta^{18}O$ values of meteoric precipitation, and which, in many

272 locations, are linked to climate (air temperature, moisture source, seasonality of precipitation, or

273 rainfall amount). Oxygen isotopic ratios in stalagmites primarily reflect the $\delta^{18}O$ value of

274 effective precipitation, as only an extremely small proportion of oxygen in dripwater is

275 contributed by dissolution of CO_2 or bedrock carbonate (Lachniet, 2009). Interpreting changes in

276 oxygen isotope composition at BG/GCL during intervals of profound climatic change such as

277 marked the last glacial period is complicated by the multiple factors that influenced $\delta^{18}O$ values

278 of precipitation at these sites, including shifts in moisture source. The potential exists for rainfall

279 in Iberia to be derived from atmospheric moisture sources that change on synoptic/seasonal

280 scales (Moreno et al., 2014; Gimeno et al., 2010; Gimeno et al., 2012) as well as in response to

281 changing glacial boundary conditions (Florineth and Schlüchter, 2000; Kuhlemann et al., 2008;

282   Luetscher et al., 2016). In addition, strong but opposite correlations exist in modern precipitation

283   between rainwater $\delta^{18}O$ values and (i) the regional air temperature (r=+0.8) and (ii) rainfall

284   amount (r=-0.8), both of which are related to the strong seasonality of precipitation associated

285   with Meso-Mediterranean climates (IPMA, 2016).

286   Stalagmite $\delta^{13}C$ values reflect two primary inputs: CO_2 derived from the atmosphere

287   and/or soil zone and bicarbonate derived from dissolution of bedrock carbonate. Speleothem

288     $\delta^{13}C$ values reflect the type (C_3 vs C_4) and density of vegetation over the cave, both of which are

289   impacted by changes in air temperature and/or precipitation. The average $\delta^{13}C$ value of biogenic

290   CO_2 in the soil zone is tied to the ratio of plants utilizing the C_3 (average $\delta^{13}C$ -26‰) versus C_4

291   (average $\delta^{13}C$ -14‰) photosynthetic pathways (Deines, 1980; von Fischer et al., 2008).

292   Similarly, vegetation density and soil respiration rates over the cave impact the relative

293   contribution of atmospheric CO_2 (pre-Industrial $\delta^{13}C$ -6‰ to -7‰; Francey et al., 1999) as

294   compared to soil-derived CO_2 (Hellstrom and McCulloch, 2000; Genty et al., 2003). Phanerozoic

295   bedrock $\delta^{13}C$ values range from -4‰ to +8‰ (Saltzman and Thomas, 2012), but these values are

296   static and do not contribute to temporal variability in stalagmite carbon isotopic ratios.

297   Superimposed on these inputs are secondary effects capable of influencing the $\delta^{13}C$

298   values of dripwater in the epikarst or cave. When voids in the bedrock are not fully saturated,

299   CO_2 degassing from infiltrated water may occur in the epikarst. This preferential loss of $^{12}CO_2$

300   (that may result in crystallization of calcium carbonate – so-called prior calcite precipitation)

301   enriches the residual solution in ^{13}C, a signal that can be transferred into underlying stalagmites

302   (Baker et al., 1997). Once the solution enters the cave, equilibrium fractionation between

303   dissolved carbon species may be disrupted owing to issues surrounding CO_2-degassing under

304   low drip rate conditions (Breitenbach et al., 2015) or by disequilibrium processes occurring

305   during carbonate crystallization (Mickler et al., 2004; Fairchild et al., 2006). Importantly, $\delta^{13}C$

306   reflect local infiltration rather than (pan-)regional atmospheric conditions as in the case of $\delta^{18}O$.

307   This difference between both proxies offers the opportunity to investigate environmental changes

308   at different spatial scales.

309   Correlations between carbon and oxygen isotope ratios are presented in Figure 8. Three

310   stalagmites – BG6LR, BG66, and BG67 – show strong correlations between $\delta^{13}C$ and $\delta^{18}O$

311   (r^2=0.6), while the other three samples lack significant correlation. If one considers the second

312   criterion of the Hendy Test, the nature of equilibrium crystallization in stalagmites BG6LR,

313   BG66, and BG67 would be considered suspect. It must be noted, however, that the reliability of

314   the Hendy Test has been questioned because (1) equilibrium may be maintained in some portions

315   of a stalagmite but not others, (2) growth layers thin progressively down the sides of the

316   stalagmite, making it difficult to restrict samples to the same material, and (3) equilibrium

317   covariation of carbon and oxygen isotope ratios may result as the direct or indirect result of

318   climatic variability (Dorale and Liu, 2009; Lechleitner et al., 2017). We therefore interpret both

319   isotope ratios and their covariation as environmental signals.

320   An additional test of equilibrium crystallization in the modern system can be constructed

321   by comparing modeled stalagmite isotopic values to recently deposited calcite. The carbon

322   isotopic composition of speleothem calcite is the result of a complex series of reactions that have

323   been addressed in a number of studies (Hendy, 1971; Mühlinghaus et al., 2007; Dreybodt, 2008).

324   For $\delta^{13}C$ in BG stalagmites, we use the equations of Li et al. (2014), which factor in the two

325   primary sources of carbon – soil CO_2 and bedrock carbonate – the proportion of carbon derived

326   from each source, and temperature-induced fractionation of carbon isotopes between dissolved

327   carbon species:

328

329     $\delta^{13}C_{calcite} = f_1 * [\delta^{13}C_{ls} - (\delta^{13}C_{CO2(g)} + 9.48 \times 10^3/T - 23.89)] + \delta^{13}C_{CO2(g)} + 9.48 \times 10^3/T + 0.049T - 37.72$

330

331   where: f_1 = fraction of bicarbonate from limestone

332   ls = limestone

333   T = temperature (˚K)

334

335   We assume the most straightforward and simple situation: the system remains closed to

336   soil CO_2 and bedrock carbonate contributes 50% of carbon to dripwater bicarbonate (f_1=0.5). We

337   apply the average cave temperature of 14.4˚C and the measured $\delta^{13}C$ values of BG bedrock and

338   the overlying vegetation/soil of +3±1‰ and -28±1‰, respectively. This approach, while

339   certainly overly simplified for the BG system, yields modeled stalagmite $\delta^{13}C$ values of -

340   7.7±1‰, similar to calcite crystallized on two glass slides installed at the site of two actively

341   growing stalagmites in the loft area of BG, which yielded $\delta^{13}C$ values of -8.4±1.2‰.

342   Oxygen isotopic ratios were modeled using the paleotemperature equation of Kim and

343   O'Neil (1997), which requires measurements of cave temperature and dripwater δ^{18}O values.

344   The modeled δ^{18}O value of -3.1±1.0‰ is nearly identical to the glass plate calcite value of -

345   3.0±0.6‰. It should be noted, however, that assessing equilibrium crystallization in modern

346   calcite/dripwater pairs at BG is complicated by the low temporal resolution associated with

347   integrated, months-long dripwater samples, variable timing of dripwater collecting trips, and any

348   seasonal biases in calcite crystallization that at present remain poorly constrained.

349   Replication between stalagmites of similar age is arguably the single most reliable

350   method for evaluating the impacts of climate versus secondary influences, including evaporation

351   and kinetic effects (Denniston et al., 1999; Mickler et al., 2004), on stalagmite isotopic ratios

352   (Dorale and Liu, 2009; Denniston et al., 2013). When presented as an integrated data set, the

353   BG/GCL stalagmite carbon and oxygen isotopic time series spans the majority of the last 230 ka

354   (Fig. 9), although stalagmites spanning the same periods of time are restricted to 187-185, 111-

355   104, 83-81, 78-73, and 58-53 ka. Because these intervals are short, and because the temporal

356   resolution varies substantially between stalagmites, replication tests based on these intervals are

357   of limited utility. Within the age uncertainties, δ^{18}O and δ^{13}C values and trends are similar,

358   suggesting that oxygen and carbon isotopic ratios track environmental, rather than drip-specific,

359   variables. The three exceptions in which coeval samples do not replicate well are: δ^{13}C values

360   offset by 3‰ from 83-81 ka and by 4‰ from 58-53 ka, and δ^{18}O values offset by 1‰ from 111-

361   104 ka (Fig. 9; Supp. Fig. S4).

362

363   *4.4 Hydroclimate Proxies*

364   *4.4.1 Carbon Isotopes*

365   Interpreting speleothem δ^{13}C variability in a climatic context requires understanding, or

366   at least constraining, the origins of these isotopic shifts. Terrestrial deposits preserving pollen

367   spectra spanning substantial portions of the last glacial cycle from western Iberia are rare

368   (Gómez-Orellana et al., 2008; Fletcher et al., 2010; Moreno et al., 2012), and thus pollen in

369   marine sediments represents a particularly important continental climate record. Pollen samples

370   obtained from the Iberian margin contain small percentages of *Poaceae*, the family including the

371   majority of C_4 plants, demonstrating a persistent and overwhelming majority of C_3 (largely shrub

372   and arboreal) vegetation throughout the last glacial cycle including between Greenland stadials

373   (GS) and interstadials (GI) and across Heinrich stadials (HS) (d'Errico and Sánchez Goñi, 2003;

374   Tzedakis et al., 2004; Desprat et al., 2006; Sánchez Goñi et al., 2008; Sánchez Goñi et al., 2013;

375   Margari et al., 2014). In the absence of changes in vegetation type, shifts in the source of carbon

376   found in cave dripwater therefore likely originated with the density of vegetation and/or soil

377   respiration rates (Genty et al., 2003). Reductions in these values are generally associated with

378   decreases in temperature and/or increases in aridity, such as have been inferred from Iberian

379   pollen spectra to have characterized Iberia during GS, HS, and glacial maxima (Sánchez Goñi et

380   al., 2008; Margari et al., 2014). Complementing these effects are increases in the contribution of

381   bedrock carbon, as well as prior calcite precipitation, reflecting a combination of longer

382   residence times of infiltrating solutions and desaturation of voids in the epikarst above the cave,

383   both of which are consistent with more arid climates (Baker et al., 1997; Genty et al., 2003).

384   Thus, we interpret the carbon isotopic values of the BG/GCL record as primarily a local

385   (hydro)climate proxy, with higher $\delta^{13}C$ values indicative of a cooler, drier climate. Integrating

386   the GCL6 $\delta^{13}C$ record into the BG time series is complicated by the slightly different bedrock

387    $\delta^{13}C$ values of the host rocks (Supp. Table 1) and what may have been distinct vegetation types

388   and cave hydrologies at each cave when GCL6 was being deposited (187-160 ka). However, as

389   previously discussed, the similar $\delta^{13}C$ values during their period of overlap (187-185 ka)

390   suggests that the two records can be consolidated.

391

392   *4.4.2 Oxygen Isotopes*

393   The origins of BG/GCL isotopic variability appear more complex for oxygen than for

394   carbon. Like $\delta^{13}C$ values, local $\delta^{18}O$ minima mark interstadials and interglacials. Analysis of

395   modern precipitation data reveals equally strong, albeit inverse, correlations between

396   precipitation $\delta^{18}O$ and both amount (r=-0.8) and air temperature (r=+0.8) effects, likely owing to

397   the dominance of cool season precipitation in annual water budgets (IAEA/WMO, 2016) (Fig.

398   2). Based on these relationships, it remains possible that changes in air temperature, overall

399   precipitation, and/or precipitation seasonality could impact the $\delta^{18}O$ values of effective moisture.

400   That air temperature is likely not a prominent driver of oxygen isotopic variability is supported

401   by two observations, however. First, the slope of the air temperature/$\delta^{18}O$ relationship

402   (+0.2‰/˚C) is nearly identical, but opposite in sign, to the calcite-water temperature dependence

403   of oxygen isotopic fractionation (-0.2‰/˚C) (Kim and O'Neil, 1997). In the simplest sense,

404   therefore, a 1˚C increase in mean annual air temperature (and thus also cave temperature) would

405   increase precipitation δ^{18}O values by approximately the same amount that the water temperature

406   effect would lower stalagmite calcite δ^{18}O values. In this simplified scenario, the net effect is a

407   stalagmite record that is negligibly influenced by temperature changes alone. Secondly, the

408   observed shift toward lower stalagmite δ^{18}O values during interstadials and interglacials, periods

409   of elevated mean annual temperature, demonstrates that the observed positive correlation

410   between precipitation δ^{18}O and air temperature is not a dominant feature over millennial time

411   scales. For example, the 3.5‰ decrease in δ^{18}O values between MIS 6 and MIS 5e (136-128 ka)

412   (Fig. 9) can be only partially accounted for by the ~1‰ ice volume-related decrease in North

413   Atlantic surface water δ^{18}O values (Schrag et al., 1996). Other factors such as kinetics associated

414   with humidity and wind speed at the point of evaporation (Grootes et al., 1993), temperature and

415   source of atmospheric moisture (Herbert et al., 2001), and cloud evolutionary pathways

416   (Rozanski and Araguás, 1995) need also be considered but cannot account for the entirety of this

417   shift. Because of the narrow continental shelf in central Portugal, the LGM shoreline was located

418   close to the modern shoreline, thereby minimizing continental effects, and the magnitude of the

419   impacts of wind speed and ocean temperature do not appear sufficient to account for the

420   observed stalagmite δ^{18}O variability. Thus, the decrease in stalagmite δ^{18}O between the

421   penultimate glacial and last interglacial suggests that stalagmite oxygen isotope ratios are

422   primarily recording (pan-)regional hydroclimate rather than temperature.

423

424   *4.4.3 δ^{234}U Values*

425   δ^{234}U values (calculated as the difference between the age-corrected ^{234}U/^{238}U ratio of a

426   sample and the secular equilibrium ^{234}U/^{238}U ratio) of speleothem carbonate has also been used

427   as a proxy for paleoprecipitation (Hellstrom and McCulloch, 2000; Oster et al., 2012; Plagnes et

428   al., 2002; Polyak et al., 2012; Zhou et al., 2005). ^{234}U exists in the stalagmite crystalline lattice

429   due to incorporation from cave dripwater and through *in situ* production from decay of ^{238}U.

430   Alpha recoil displaces ^{234}U from its lattice position, increasing its susceptibility to leaching by

431   infiltrating waters, meaning that ^{234}U is selectively mobilized relative to ^{238}U in cave dripwater

432   (Chabaux et al., 2003; Oster et al., 2012). The flux of infiltrating fluids is therefore tied to δ^{234}U

433   values of dripwater, and thus stalagmite carbonate such that decreases in effective precipitation

434   and/or bedrock dissolution rate, both of which are tied to increased aridity, are associated with

435   elevated speleothem δ^{234}U values (Hellstrom and McCulloch, 2000; Plagnes et al., 2002; Polyak

436   et al., 2012).

437   As differences in δ^{234}U values between stalagmites may arise from distinct infiltration

438   pathways (Zhou et al., 2005), complicating the integration of δ^{234}U values from multiple

439   stalagmites into a single, cohesive data set, we restrict our analysis to stalagmite BG6LR, which

440   represents the longest individual stalagmite record of the BG/GCL time series. While the number

441   of δ^{234}U measurements is small compared to stable isotopic values, the temporal density of the

442   former is sufficient to demonstrate the utility of δ^{13}C and δ^{18}O values as paleohydroclimate

443   proxies (Fig. 9). Decreased precipitation/effective moisture is associated with elevated stalagmite

444   δ^{13}C, δ^{18}O, and δ^{234}U values. The relationships between δ^{13}C and δ^{234}U values in all BG and

445   GCL stalagmites are presented in Supp. Fig. S5.

446

447   **5. Environmental Conditions at BG/GCL and Links to Iberian Margin SST**

448   The previously discussed tests for isotopic equilibrium, including the reproducibility of

449   carbon and oxygen isotope ratios between coeval BG and GCL stalagmites, support the notion

450   that their δ^{13}C and δ^{18}O values may be integrated into cohesive time series reflecting

451   paleohydroclimatic conditions and used to assess links between continental climate and SST

452   (Fig. 10). Over the last several glacial cycles, oceanographic conditions along the western Iberian

453   margin varied at millennial and orbital time scales in close correlation with Greenland air

454   temperature and North Atlantic conditions and circulation (Roucoux et al., 2005; Daniau et al.,

455   2007; Sánchez Goñi et al., 2008; Darfeuil et al., 2016). Abrupt changes in SST reflect a balance

456   between southward expansion of subpolar waters and northward migration of subtropical water

457   masses (de Abreu et al., 2003). During the particularly cold conditions characterizing HS and

458   GS, Iberian margin SST decreased by up to 9˚C (to as much as 13˚C below present values; de

459   Abreu et al., 2003), with these changes helping to position the arctic or subarctic front at ~39˚N,

460   the same latitude as BG and GCL. These cold surface waters reduced the production and

461   transport of atmospheric moisture to Iberia (Eynaud et al., 2009; Voelker and de Abreu, 2011),

462   and would have thereby influenced the timing of speleothem growth and carbon and oxygen

463   isotopic values in BG and GCL stalagmites. Indeed, the composite BG/GCL record documents

464   coherence, at both orbital and millennial scales, between Portuguese hydroclimate, vegetation,

465 and Iberian margin SST during the last two glacial cycles (Fig. 10 and 11). In an attempt to

466 quantify this covariance, we binned the SST and stalagmite stable isotope data into century-long

467 intervals. The relatively short record of BG41 was not included, and model ages for stalagmites

468 BG66 and GLC6 were increased by 4.0 kyr and 1.3 kyr, respectively, to improve correlation with

469 the SST chronology. The resulting inverse correlation between SST and carbon and oxygen is

470 strong (r=-0.55 and -0.52, respectively; p<0.0001) (Supp. Fig. S6).

471

472 *5.1 Growth Intervals*

473   The single most fundamental prerequisite to speleothem deposition is infiltration of

474 surface waters, and thus the timing of stalagmite growth can reflect changes in mean

475 hydroclimatic state. Deposition of multiple BG stalagmites was punctuated by hiatuses spanning

476 similar time intervals (although the precise ages of the onset and/or termination of the hiatuses

477 are distinct), a relationship that suggests links to changes in hydroclimate rather than random

478 drip site-specific variability.

479   Hiatuses in some BG samples coincide with HS1, HS3, HS4, and HS6, and pollen spectra

480 independently suggest increased aridity during HS and glacial maxima. Decreases in arboreal

481 pollen abundance and concomitant increases in drought-tolerant vegetation coincide with periods

482 of reduced SST. Vegetation patterns during maximal IRD deposition on the Iberian margin

483 reveal not only dramatically reduced forest cover but also a pronounced expansion of semi-desert

484 plants (e.g. Sánchez Goñi et al., 2000; Roucoux et al., 2005; Naughton et al., 2009). These

485 changes mark the long hiatus between HS7 and HS6 (71-59 ka), which overlaps with the some of

486 the coldest SST of the last 70 ka as reconstructed using $U_{37}^{k'}$ at core MD95-2042 (Darfeuil et al.,

487 2016) (Fig. 10; Fig. 12). An absence in BG stalagmite deposition from ~160-149 ka occurs at the

488 same time as massive seasonal discharges from the Fleuve Manche river and the coldest

489 continental climates and SST (157-154 ka) of the last 230 ka, as determined from pollen and

490 foraminifera from core MD01-2444 (Margari et al., 2014; Fig. 1).

491   Whether hiatuses in BG speleothem deposition are a result of pronounced reductions in

492 precipitation, an extension of below freezing temperatures that limited infiltration (Vaks et al.,

493 2013; Fankhauser et al., 2016), or variations in infiltration pathway/drip position is ambiguous.

494 Pollen transfer functions from MD95-2042 suggest winter temperatures dropped below 0˚C

495 during HS and annual precipitation was reduced by up to 50% (from 800 mm to 500-400 mm

496   during HS3, HS4, and HS5) (Sánchez Goñi et al., 2002). Applying this temperature

497   reconstruction to western Portugal is complicated, however, by the broad area across which these

498   pollen were sourced. Permafrost reconstructions (Vandenberghe et al., 2014) of Iberia argue

499   against the hypothesis that continuous sub-zero temperatures inhibited infiltration and stalagmite

500   growth. We thus suggest that the hiatuses observed at BG and GCL were driven largely by

501   reductions in precipitation.

502   Other western European cave records also share similar growth histories. For example,

503   stalagmites from Villars Cave, southwestern France (Genty et al., 2003; Genty et al., 2010;

504   Wainer et al., 2011), and from multiple caves in northern Spain (Stoll et al., 2013) (Fig. 1) are

505   also punctuated by hiatuses during HS. For example, at or near HS7, stalagmite hiatuses were

506   formed at Villars Cave (78-76 ka), in northern Spain (~75 k), and BG (80-78 ka). No stalagmite

507   deposition has been identified at BG from 71-60 ka or Villars cave from 67-62 ka, a period that

508   includes HS6. Finally, HS1 is marked by a hiatus in northern Spain (18-15.5 ka) and at BG (17-

509   15 ka). While the timing of these hiatuses is not identical, and not all hiatuses at Villars Cave and

510   the Spanish caves overlap with those at BG, the substantial degree of overlap suggests a common

511   origin. Stoll et al. (2013) noted that stalagmite deposition and/or elevated growth rates in

512   northern Spain stalagmites occurred during periods of high Northern Hemisphere summer

513   insolation or during GI, while hiatuses occurred during periods of low insolation and low SST

514   (<13.7˚C). The BG record supports this interpretation that growth interruptions are most likely

515   related to reductions in effective moisture tied to SST controls on regional atmospheric moisture

516   availability.

517

518   *5.2 BG/GCL Stable Isotopic and $\delta^{234}U$ Variability*

519   Stalagmite $\delta^{13}C$ and $\delta^{18}O$ values covary with changes in SST at orbital time scales. The

520   offset between interglacial and glacial isotopic values averages ~3‰ for $\delta^{18}O$ and ~7‰ for $\delta^{13}C$

521   values and largely tracks changes in NH summer insolation (Fig. 10). Stalagmite $\delta^{234}U$ values

522   also preserve these changes in aridity. Millennial-scale changes are also recorded in stalagmite

523   carbon isotope ratios, with shifts of 3-7‰ associated with GI/GS transitions, and oxygen isotopic

524   changes of ~1-2‰. The large swing in $\delta^{18}O$ values during the transition from GI-1 to the

525   Younger Dryas (YD) (~5‰ from 14.0-13.5 ka) is anomalous. Given that the change in $\delta^{13}C$

526   values at this time (6‰) is consistent with other GI transitions, the hydroclimatic implications of

527   this interval require additional study. Similarly, oxygen and carbon isotopic variability is
528   pronounced during the late Holocene portion of the BG record. The origin of this high variability
529   is unclear although it could simply represent the considerably faster Holocene stalagmite growth
530   rates, and thus reduced time averaging in stable isotope samples, relative to the Pleistocene
531   sections, or possibly external factors such as a change in cave ventilation that increased
532   evaporation may be involved. Replication of the Holocene portion of this record currently
533   underway will help address this question (Thatcher et al., 2018).

534   Where growth is continuous during HS, the link between stalagmite isotopic variations
535   and SST changes is clearly visible (Fig. 11). Prominent positive carbon isotopic excursions
536   define the YD, HS2, HS5, HS6, and HS8, consistent with diminished concentrations of arboreal
537   pollen in cores from the Iberian margin, and serve to document particularly cold and dry
538   conditions at these times (Sánchez Goñi et al., 2000; Roucoux et al., 2006; Sánchez Goñi et al.,
539   2008). Reduced stalagmite δ^{13}C values mark periods of enhanced effective moisture from 170-
540   160 and 145-135 ka, tracking peaks in temperate tree pollen and alkenone-based SST. The BG
541   records reveals a pronounced increase in stalagmite δ^{13}C values during the YD, at odds with the
542   plateau in SST observed in some Portuguese coastal margin sediments at this time. However, a
543   higher resolution SST record reveals a pronounced drop in SST (Rodrigues et al., 2010), well
544   matched with the BG isotopic profile and the stalagmite record from Villars Cave.

545   Hydroclimatic shifts associated with GS and GI are most clearly expressed during MIS
546   5a and 5b in the BG carbon isotope record (Fig. 11). Other European stalagmite records have
547   identified GI/GS events from the last glacial period (Genty et al., 2003; Spötl et al., 2006; Boch
548   et al., 2011; Moseley et al., 2014) (Fig. 10), but the level of resolution recorded in the BG/GCL
549   time series has not been clearly identified previously in western Iberia. A carbon isotope time
550   series (albeit with low temporal resolution) of a flowstone from southeastern Spain does not
551   present clear evidence of either GI or most HS during the last glacial cycle, although it does
552   contain a clear expression of HS11 (Hodge et al., 2008) (Fig. 1). And while some Iberian lakes
553   and peat bogs document environmental changes concurrent with HS, no single record, including
554   one of the longest - the 50 ka time series from the Fuentillejo maar, south-central Spain -
555   contains a consistent signal for all HS (Vegas et al., 2010; Moreno et al., 2012) (Fig. 1). GS/GI
556   oscillations during MIS 3 are not clearly defined in BG stalagmites, likely owing to insufficient

557 temporal resolution, although the BG records does share a resemblance to reconstructed SST

558 variability (Fig. 11).

559 Whether the apparent inconsistent linkages between Iberian margin SST and Iberian

560 hydroclimate are due to the limitations of these proxies, region-specific responses to SST

561 variations, or a changing influence of SST on precipitation is unclear. However, other points of

562 divergence between SST and the BG/GCL records exist. For example, some marine cores reveal

563 a prominent spike in forest taxa occurring at the start of interglacials, decreasing thereafter for

564 the next 5-10 kyr (Tzedakis et al, 2004; Desprat et al., 2007) (Fig. 10). This early interglacial

565 peak is a common feature in several time series including the Antarctic δD (Petit et al., 1999)

566 and CH_4 records (Loulergue et al., 2008), and in stalagmite isotopic ratios from the eastern

567 Mediterranean (Bar-Matthews et al., 2003) and southern France (Couchoud et al., 2009). The

568 BG/GCL δ^{13}C and δ^{18}O records lack this feature, although the previously discussed issues

569 surrounding the continuity of the MIS6/5e transition may complicate identifying it.

570 Stalagmite δ^{13}C and δ^{18}O values are lower during GI 20-22 (MIS 5a/4; 84-72 ka) than in

571 either the Holocene or MIS 5e (Fig. 10 and 12), and BG6LR δ^{234}U values support this

572 observation. This interval is of particular interest given that Atlantic forest pollen, which has

573 been used as a proxy for air temperature, was decoupled from SST across northwestern Iberia

574 during cold events (C18-C20) (Rousseau et al., 2006; Rasmussen et al., 2014). This decoupling

575 is interpreted as reflective of a weakened control of SST on Iberian atmospheric temperature

576 that, in turn, enhanced transport of atmospheric vapor to the high latitudes, amplifying

577 production of ice sheets in the early stages of the last glacial cycle (Sánchez Goñi et al., 2013).

578 This process has also been demonstrated for an earlier interglacial (MIS 19; Sánchez Goñi et al.,

579 2016). Other offsets include (1) the gradual change in BG δ^{13}C and δ^{18}O values across the MIS

580 8/7 boundary, in contrast to the sharp rise in SST at this time; (2) the anomalously large δ^{13}C

581 response to ice rafting event C24 (111-108 ka), and (3) the persistence of low δ^{13}C values as SST

582 decreased from 205-187 ka (Fig. 11 and 12).

583 The mechanism linking SST and Iberian hydroclimate over millennial time scales

584 remains unclear. The NAO exerts a strong control over Iberian precipitation, and previous

585 studies have suggested that GS and GI (Moreno et al., 2002; Sánchez Goñi et al., 2002; Daniau

586 et al., 2007) and HS (Naughton et al., 2009) were characterized by distinct NAO modes. The

587 dynamics of the NAO and Azores High pressure system are not well understood prior to the

588 historical era (Trouet et al., 2009), and the BG/GCL record cannot address this question

589 independently. However, rainfall variability in eastern Iberia is less closely tied to the NAO than

590 is western Iberia and instead reflects other climatic phenomena including the El Niño-Southern

591 Oscillation (Rodó et al., 1997), helping to produce an east-west precipitation gradient.

592 Additional high-resolution speleothem records from central and eastern Iberia could therefore

593 provide a more robust test of the underlying drivers of millennial-scale hydroclimatic changes

594 during recent glacial periods.

595

596 **6. Conclusions**

597 The discontinuous BG/GCL speleothem composite record demonstrates that the

598 hydroclimate and vegetation dynamics in west-central Portugal tracked Iberian margin SST over

599 orbital and millennial scales during the past two glacial cycles. Enhanced aridity characterized

600 HS, as evidenced by elevated carbon and oxygen isotopic ratios and/or hiatuses in stalagmite

601 growth, consistent with other regional stalagmite time series. GI/GS variability expressed in the

602 Iberian margin SST record and in co-deposited pollen spectra are also present in the BG/GCL

603 time series, and are particularly well defined in MIS 5a and 5b. Understanding differences

604 between the structures of the stalagmite and SST records during some time intervals will require

605 development of speleothem records from central and southern Iberia.

606

607 **Acknowledgements**

608 This work was supported by the Center for Global and Regional Environmental Research

609 and Cornell College (to R.F.D.), and the U.S. National Science Foundation (grant BCS-1118155

610 to J.A.H., BCS-1118183 to M.M.B., and AGS-135539 to C.C.U.). Field sampling performed

611 under the auspices of IGESPAR (to J.A.H.) and Associação de Estudos Subterrâneos e Defesa do

612 Ambiente. Brandon Zinsious and Stephen Rasin contributed to fieldwork at BG, and Zachary

613 LaPointe assisted with radioisotopic analyses; Suzanne Ankerstjerne performed stable isotope

614 measurements. Use of the following data sets is gratefully acknowledged: Global Precipitation

615 Climatology Center data by the German Weather Service (DWD) accessed

616 through http://gpcc.dwd.de; NAO Index Data provided by the Climate Analysis Section, NCAR,

617 Boulder, USA, Hurrell (2003). Updated regularly. Accessed through

618 https://climatedataguide.ucar.edu/climate-data/hurrell-north-atlantic-oscillation-nao-index-pc-

619 based. This manuscript benefitted from discussions with Maria F. Sánchez Goñi, David Hodell,

620 and Chronis Tzedakis. We thank four anonymous reviewers, whose detailed and thoughtful

621 assessment of the original version of this manuscript substantially improved its scope and clarity.

622 Stable and U-series isotope data are available at the NOAA National Centers for Environmental

623 Information website.

624

References

626 de Abreu, L., Shackleton, N.J., Schönfeld, J., Hall, M., and Chapman, M.: Millennial-scale

627   oceanic climate variability off the Western Iberian margin during the last two glacial periods,

628   Marine Geol, 196, 1-20, 2003.

629 Asmerom, Y., Polyak, V., Burns, S.: Variable winter moisture in the southwestern United States

630   linked to rapid glacial climate shifts, Nat Geosci, 3, 114-117, 2010.

631 Baker, A., Ito, E., Smart, P., McEwan, R.: Elevated and variable values of ^{13}C in speleothems in

632   a British cave system, Chem Geol, 136, 263-270, 1997.

633 Barker, S., Knorr, G., Edwards, R.L., Parrenin, F., Putnam, A.E., Skinner, L.C., Wolff, E.,

634   Ziegler, M.: 800,000 years of abrupt climate variability, Science, 334, 347-351, 2011.

635 Bar-Matthews, M., Ayalon, A., Gilmour, M., Matthews, A., Hawkesworth, C.J.: Sea-land

636   oxygen isotopic relationships from planktonic foraminifera and speleothems in the Eastern

637   Mediterranean region and their implication for paleo-rainfall during interglacials intervals,

638   Geochim Cosmochim Ac, 67, 3181–3199, 2003.

639 Barnston, A.G. and Livezey, R.E.: Classification, seasonality, and persistence of low-frequency

640   atmospheric circulation patterns, Mon Weather Rev, 115, 1083–1126, 1987.

641 Berger, A. and Loutre, M.F.: Insolation values for the climate of the last 10 million years.

642   Quaternary Sci Rev 10, 297-318, 1991.

643 Blanco Castro, E., Casado González, M.A., Costa Tenorio, M., Escribano Bombín, R., García

644   Antón, M., Génova Fuster, M., Gómez Manzaneque, F., Gómez Manzaneque, A., Moreno

645   Sáiz, J.C., Morla Juaristi, C., Regato Pajares, P., Sáiz Ollero, H.: Los bosques ibéricos.

646   Planeta, Barcelona, 1997.

647 Boch, R., Cheng, H., Spötl, C., Edwards, R.L., Wang, X., Hauselmann, Ph.: NALPS: a precisely

648   dated European climate record 120-60 ka, Clim Past, 7, 1049-1072, 2011.

649 Breitenbach, S.F.M., Rehfeld, K., Goswami, B., Baldini, J.U.L., Ridley, H.E., Kennett, D.J.,
650   Prufer, K.M., Aquino, V.V., Asmerom, Y., Polyak, V.J., Cheng, H., Kurths, J., Marwan, N.:
651   Constructing proxy records from age models (COPRA), Clim Past, 8, 1765-1779, 2012.

652 Breitenbach, S.F.M., Lechleitner, F.A., Meyer, H., Diengdo, G., Mattey, D., Marwan, N.: Cave
653   ventilation and rainfall signals in dripwater in a monsoonal setting – a monitoring study from
654   NE India, Chem Geol, 402, 111-124, 2015.

655 CDG: The Climate Data Guide: Hurrell North Atlantic Oscillation (NAO) Index (PC-based).
656   Retrieved   from https://climatedataguide.ucar.edu/climate-data/hurrell-north-atlantic-
657   oscillation-nao-index-pc-based, accessed 21 May, 2018.

658 Chabaud, L., Sánchez Goñi, M.F., Desprat, S., Rossignol, L.: Land-sea climatic variability in the
659   eastern North Atlantic subtropical region over the last 14,200 years: Atmospheric and
660   oceanic processes at different timescales Holocene, 24, 787-797, 2014.

661 Chabaux, F., Riotte, J., Dequincey, O.: U–Th–Ra fractionations during weathering and river
662   transport. Rev Mineral Geochem, 52, 533–576. 2003.

663 Collister, C. and Mattey, D.: Controls on water drop volume at speleothem drip sites: An
664   experimental study. J Hydrol, 358, 259-267, 2008.

665 Combourieu-Nebout, N., Peyron, O., Dormoy, I., Desprat, S., Beaudouin, C., Kotthoff, U.,
666   Marret, F.: Rapid climatic variability in the west Mediterannean during the last 25 000 years
667   from high resolution pollen data, Clim Past, 5, 503-521, 2009.

668 Cortesi, N., Gonzalez-Hidalgo, J.C., Trigo, R.M., and Ramos, A.M.: Weather types and spatial
669   variability of precipitation in the Iberian Peninsula. International Journal of Climatology, 34,
670   2661-2677, 2014.

671 Couchoud, I, Genty, D., Hoffman, D., Drysdale, R., Blamart, D.: Millennial-scale climate
672   variability during the Last Interglacial recorded in a speleothem from south-western France.
673   Quaternary Sci Rev, 28, 3263-3274, 2009.

674 Daniou, A.-L., Sánchez Goñi, M.F., Beaufort, L., Laggoun-Defarge, F., Loutre, M.-F., Duprat,
675   J.: Dansgaard-Oeschger climatic variability revealed by fire emissions in southwestern Iberia.
676   Quaternary Sci Rev, 26, 1369-1383, 2007.

677 Darfeuil, S., Ménot, G., Giraud, X., Rostek, F., Tachikawa, K., Garcia, M., Bard, É.: Sea surface
678   temperature reconstructions over the last 70 kyr off Portugal: Biomarker data and regional
679   modeling, Paleocean, 31, 40–65, 2016.

680   Deines, P.: The isotopic composition of reduced organic carbon. Handbook of Environmental

681   Isotope Geochemistry, The Terrestrial Environment, Part A (Fritz, P. and Fontes, J., Eds.,

682   Elseveier, New York, 331-406, 1980.

683   Denniston, R.F., González, L.A., Asmerom, Y., Baker, R.G., Reagan, M.K. Bettis, E.A. III.:

684   Evidence for increased cool season moisture during the middle Holocene, Geology, 27, 815-

685   818, 1999.

686   Denniston, R.F., Wyrwoll, K.-H., Polyak, Brown, J. Asmerom, Y., Wanamaker, A. Jr., LaPointe'

687   Z., Ellerbroek, R., Barthelmes, M., Cleary, D., Cugley, J., Woods, D., Humphreys, W.: A

688   Stalagmite Record of Holocene Indonesian-Australian Summer Monsoon Variability from

689   the Australian Tropics. Quaternary Sci Rev 78, 155-168, 2013.

690   Desprat et al.: Climatic variability of Marine Isotope Stage 7: direct land-sea-ice correlation from

691   a multiproxy analysis of a north-western Iberian margin deep-sea core. Quaternary Sci Rev

692   25, 1010-1026, 2006.

693   Desprat, S., Sánchez Goñi, M.F., Naughton, F., Turon, J.-L., Duprat, J., Malaizé, B., Cortijo, E.,

694   Peypouquet, J.-P.: Climate variability of the last five isotopic interglacials: Direct land-sea-

695   ice correlation from the multiproxy analysis of North-Western Iberian margin deep-sea cores,

696   Editor(s): F. Sirocko, M. Claussen, M.F. Sánchez Goñi, T. Litt *In* Developments in

697   Quaternary Sciences, Elsevier, pp. 375-386, 2007.

698   Dorale, J.A., and Liu, Z.: Limitations of Hendy Test criteria in judging the paleoclimatic

699   suitability of speleothems and the need for replication. J Cave Karst Stud, 71, 73-80, 2009.

700   Dreybodt, W.: Evolution of the isotopic composition of carbon and oxygen in a calcite

701   precipitating H_2O-CO_2-$CaCO_3$ solution and the related isotopic composition of calcite in

702   stalagmites. Geochim. Cosmochim. Acta, 72, 4712-4724, 2008.

703   Eynaud et al.: Position of the Polar Front along the western Iberian margin during key cold

704   episodes of the last 45 ka, Geochem Geophy Geosys, 10, Q07U05,

705   doi:10.1029/2009GC002398, 2009.

706   Fairchild, I.J., Smith, C.L., Baker, A., Fuller, L., Spötl, C., Mattey, D., McDermott, F., E.I.M.F.:

707   Modification and preservation of environmental signals in speleothems. Earth Sci Rev 75,

708   105-153, 2006.

709   Fankhauser, A., McDermott, F., and Fleitmann, D.: Episodic speleothem deposition tracks the

710   terrestrial impact of millennial-scale last glacial climate variability in SW Ireland, Quaternary

711   Sci Rev, 152, 104-117, 2016.

712   von Fischer, J.C., Tieszen, L.L., and Schimel, D.S.: Climate controls on C_3 vs. C_4 productivity in

713   North American grasslands from carbon isotope composition of soil organic matter. Global

714   Change Bio, 14, 1–15, 2008.

715   Fletcher, W.J., Sánchez Goñi, M.F., Allen, J.R.M., Cheddadi, R., Combourieu-Nebout, N.,

716   Huntley, B., Lawson, I., Londiex, L., Magri, D., Margari, v., Müller, U.C., Naughton, F.,

717   Novenko, E., Roucoux, K., Tzedakis, P.C.: Millennial scale variability during the last glacial

718   in vegetation records from Europe. Quaternary Sci Rev, 29, 2839-2864, 2010.

719   Florineth, D. and Schlüchter, S. Alpine Evidence for Atmospheric Circulation Patterns in Europe

720   during the Last Glacial Maximum. Quaternary Research, 54, 295-308, 2000.

721   Francey, R. J., Allison, C. E., Etheridge, D. M., Trudinger, C. M., Enting, I. G., Leuenberger, M.,

722   Langenfelds, R. L., Michel, E., and Steele, L. P. A.: 1000-year high precision record of ^{13}C in

723   atmospheric CO_2. Tellus B: Chemical and Physical Meteorology, 51, 170-193, 1999.

724   Genty, D., Blamart, D., Ouahdi, R., Gilmour, M., Baker, A., Jouzel, J., Van-Exter, S.: Precise

725   dating of Dansgaard-Oeschger climate oscillations in western Europe from stalagmite data,

726   Nature, 421, 833-837, 2003.

727   Genty, D., Comboruieu-Nebout, N., Peyron, O., Blamart, D., Wainer, K., Mansuri, F., Ghaleb,

728   B., Isabello, L., Dormoy, I., von Grafenstein, U., Bonelli, S., Landais, A., Brauer, A.:

729   Isotopic characterization of rapid climatic events during OIS3 and OIS4 in Villars Cave

730   stalagmites (SW-France) and correlation with Atlantic and Mediterranean pollen records.

731   Quaternary Sci. Rev., 29, 2799-2820, 2010.

732   Genty, D., Blamart, D., Ghaleb, B., Plagnes, V., Causse, Ch., Bakalowicz, M., Zouari, K., Chkir,

733   N., Hellstrom, J., Wainer, K., and Bourges, F.: Timing and dynamics of the last deglaciation

734   from European and North African δ^{13}C stalagmite profiles – comparison with Chinese and

735   South Hemisphere stalagmites. Quaternary Sci Rev 25, 2118-2142, 2006.

736   Gimeno, L., Nieto, R., Trigo, R.M., Vicente-Serrano, S.M., and López-Moreno, J.I., Where does

737   the Iberian Peninsula moisture comr from? An answer based on a Lagrangian approach. J.

738   Hydrometeorology, 11, 421-436, 2010.

739   Gimeno, L., Stohl, A., Trigo, R.M., Dominguez, F., Yoshimura, K., Yu., L., Drumond,A.,

740   Durán-Quesada, A.M., Nieto, R.: Oceanic and terrestrial sources of continental precipitation.

741   Rev Geophy, 50, 1-41, 2012.

742   Gómez-Orellana, L., Ramil-Rego, P., & Sobrino, C. M.: The Würm in NW Iberia, a pollen

743   record from Area Longa (Galicia). Quaternary Res, 67, 438-452, 2008.

744   Grootes, P. M.: *Climate Change in Continental Isotopic Records*, P. K. Swart, K. C. Lohmann, J.

745   McKenzie, S. Savin, Eds. (American Geophysical Union, Washington, DC), pp. 37- 46,

746   1993.

747   Hellstrom, J. and McCulloch, M.: Multi-proxy constraints on the climatic significance of trace

748   element records from a New Zealand speleothem. Earth Planet Sci Lett, 179, 287-297, 2000.

749   Hendy, C.: The isotopic geochemistry of speleothems – I. The calculation of the effects of

750   different modes of formation on the isotopic composition of speleothems and their

751   applicability as palaeoclimatic indicators. Geochimica et Cosmochica Acta 35, 801-824,

752   1971.

753   Herbert, T.D., Schuffert, J.D., Heusser, L., Lyle, M., Mix, A., Ravelo, A.C., Stott, L.D., and

754   Herguera, J.C.: Collapse of the California current during glacial maxima linked to climate

755   change on land. Science, 293, 71-76, 2001.

756   Hodell, D., Crowhurst, S., Skinner, L., Tzedakis, P.C., Margari, V., Channell, J.E.T., Kamenov,

757   G., Maclachlan, S., Rothwell, G.: Response of Iberian margin sediments to orbital and

758   suborbital forcing over the past 420 ka, Paleoceanography, 28, 185-199, 2013.

759   Hodge, E.J., Richards, D.A., Smart, P.L., Andreo, B., Hoffman, D.L., Mattey, D.P., Gonzales-

760   Ramon, A.: Effective precipitation in southern Spain (~266 to 46 ka) based on a speleothem

761   stable carbon isotope record. Quaternary Res, 69, 447-457, 2008.

762   IAEA/WMO: Global Network of Isotopes in Precipitation. The GNIP Database. Accessible at:

763   http://www.iaea.org/water, 2016.

764   IPMA: Accessible at http://www.meteo.pt/en/oclima/clima.normais/015/, 2012.

765   Justino, F. and Peltier, W.R.: The glacial North Atlantic Oscillation. Geophysical Research

766   Letters, 32, L21803, 2008.

767   Kim, S.-T. and O'Neil, J.R.: Equilibrium and nonequilibrium oxygen isotope effects in synthetic

768   carbonates: Geochim Cosmochim Ac, 61, 3461-3475, 1997.

769   Kuhlemann, J et al.: Regional synthesis of Mediterranean atmospheric circulation during the Last
770   Glacial Maximum. Science, 321, 1338– 1340, 2008.

771   Lachniet, M.S.: Climatic and environmental controls on speleothem oxygen isotope values.
772   Quaternary Sci Rev 28, 412-432, 2009.

773   Lechleitner, F.A., Breitenbach, S.F.M., Cheng, H., Plessen, B.: Climatic and in-cave influences
774   on d18O and d13C in a stalagmite from northeastern India through the last deglaciation. Quat
775   Res, 88, 458-471, 2017.

776   Li, Z-H., Driese, S.G., Cheng, H.: A multiple cave deposit assessment of suitability of
777   speleothem isotopes for reconstructing palaeo-vegetation and palaeo-temperature.
778   Sedimentology, 61, 749-766, 2014.

779   Lorenzo, M.N., Iglesias, I., Taboada, J.J., Gomez-Gesteira, M.: Relationship between monthly
780   rainfall in northwest Iberian Peninsula and North Atlantic sea surface temperature. Int J
781   Climatology, 30, 980-990, 2010.

782   Loulergue, L., Schilt, A., Spahni, R., Masson-Delmotte, V., Blunier, T., Lemieux, B., Barnola,
783   J.-M., Raynaud, D., Stocker, T.F., Chappellaz, J.: Orbital and millennial-scale features of
784   atmospheric CH4 over the past 800,000 years, Nature, 453, 383-386, 2008.

785   Luetscher, M., Boch, R., Sodemann, H., Spötl, C., Cheng, H., Edwards, R.L., Frisia, S., Hof, F.,
786   and Müller, W.: North Atlantic storm track changes during the Last Glacial Maximum
787   recorded by Alpine speleothems. Nature Communications, 6, DOI: 10.1038/ncomms7344,
788   2016.

789   Margari, V., Skinner, L.C., Tzedakis, P.C., Ganopolski, A., Vautravers, M., and Shackleton,
790   N.J.: The nature of millennial-scale climate variability during the past two glacial periods:
791   Nature Geoscience, v. 3, p. 127–131, doi:10.1038/ngeo740, 2010.

792   Margari, V., Skinner, L.C., Hodell, D.A., Martrat, B., Toucanne, S., Grimalt, J.O., Gibbard, P.L.,
793   Lunkka, J.P., Tzedakis, P.C.: Land-ocean changes on orbital and millennial time scales and
794   the penultimate glaciation, Geology, 42, 183-186, 2014.

795   Martin-Vide, J. and Lopez-Bustins, J-A.: The Western Mediterranean Oscillation and rainfall in
796   the Iberian Peninsula. Int J Climatol, 26, 1455-1475, 2006.

797   Martrat, B., Grimalt, J.O., Shackleton, N.J., de Abreu, L., Hutterli, M.A., Stocker, T.F.: Four
798   climate cycles of recurring deep and surface water destabilizations on the Iberian margin,
799   Science, 317, 502-507, 2007.

800 McManus, J.F., Oppo, D.W., Cullen, J.L.: A 0.5-Million-Year Record of Millennial-Scale
801   Climate Variability in the North Atlantic, Science, 283, 971-975, 1999.

802 Mickler, P.J. et al.: Stable isotope variations in modern tropical speleothems: Evaluation
803   equilibrium vs. kinetic isotope effects. Geochim Cosmochim Acta. 68, 4381-4393, 2004.

804 Moreno, A., Cacho, I., Canals, M., Prins, M.A., Sánchez Goñi, M.F., Grimalt, J.O., Weltje, G.J:
805   Saharan dust transport and high-latitude glacial climate variability: the Alboran Sea record.
806   Quaternary Res, 58, 318-328, 2002.

807 Moreno, A., Gonzalez-Samperiz, P., Morellon, M., Valero-Garces, B.L., Fletcher, W.J.:
808   Northern Iberian abrupt climate change dynamics during the last glacial cycle: a view from
809   lacustrine sediments. Quaternary Sci Rev, 36, 139-153, 2012.

810 Moreno, A., Sancho, C., Bartolumé, M., Oliva-Rucia, B., Delgado-Huertas, A., José, Estrela, M.,
811   Corell, D., López-Moreno, J.I., Cacho, I.: Climate controls on rainfall isotopes and their
812   effects on cave drip water and speleothem growth: the case of Molinos cave (Teruel, NE
813   Spain). Clim Dyn, 43, 221-241, 2014.

814 Moseley, G.E., Spötl, C., Scensson, A., Cheng, H., Brandstatter, S., Edwards, R.L.: Multi-
815   speleothem record reveals tightly coupled climate between central Europe and Greenland
816   during Marine Isotope Stage 3. Geology, 42, 1043-1946, 2014.

817 Mühlinghaus, C., Scholz, D., and Mangini, A.: Modelling stalagmite growth and d13C as a
818   function of drip interval and temperature. Geochim. Cosmochim. Acta, 71, 2780-2790, 2007.

819 Naughton, F., Sánchez Goñi, M.F., Desprat, S., Turon, J.-L., Duprat, J., Malaizé, B., Joli, C.,
820   Cortijo, E., Drago, T., Freitas, M.C.: Present-day and past (last 25,000 years) marine pollen
821   signal off western Iberia. Mar Micropaleontol, 62, 91–114, 2007.

822 Naughton, F., Sánchez Goñi, M.F., Kageyama, M., Bard, E., Duprat, J., Cortijo, E., Desprat, S.,
823   Malaizé, B., Joly, C., Rostek, F., Turon, J.-L.: Wet to dry climatic trend in north-western
824   Iberia within Heinrich events. Earth Planet Sc Lett, 284, 329-342, 2009.

825 North Greenland Ice Core Project members: High-resolution record of Northern Hemisphere
826   climate extending into the last interglacial period, Nature, 431, 147-151, 2004.

827 Oster, J.L., Ibarra, D.L., Harris, C.H., Maher, K.: Influence of eolian deposition and rainfall
828   amounts on the U-isotopic composition of soil water and soil minerals. Geochim Cosmochim
829   Ac, 88, 146 – 166, 2012.

830   Paredes, D., Trigo, R.M., Garcia-Herrera, R., Franco Trigo, I.: Understanding precipitation
831   changes in Iberia in early spring: weather typing and storm-tracking approaches. J
832   Hydrometeorol, 7, 101-113, 2006.

833   Petit, J.R., Jouzel, J., Raynaud, D., Barkov, N.I., Barnola, J.-M., Basile, I., Bender, M.,
834   Chappellaz, J., Davis, M., Delaygue, G., Delmotte, M., Kotlyakov, V.M., Legrand, M.,
835   Lipenkov, V.Y., Lorius, C., Pepin, L., Ritz, C., Saltzman, E., Stievenard, M.: Climate and
836   atmospheric history of the 420,000 years from the Vostok ice core, Antarctica. Nature, 399,
837   429-436, 1999.

838   Plagnes, V., Causse, C., Genty, D., Paterne, M., Blamart, D.: A discontinuous climatic record
839   from 187 to 74 ka from a speleothem of the Clamouse Cave (south of France). Earth Planet
840   Sci Lett, 201, 87-103, 2002.

841   Polyak, V.J., Asmerom, Y., Burns, S.J., and Lachniet, M.S.: Climatic backdrop to the terminal
842   Pleistocene extinction of North American mammals, Geology, 40, 1023-1026, 2012.

843   Rasmussen, S.O. et al.: A stratigraphic framework for abrupt climatic changes during the Last
844   Glacial period based on three synchronized Greenland ice-core records: redefining and
845   extending the INTIMATE event stratigraphy, Quaternary Sci Rev, 106, 14–28, 2014.

846   Rey Benayas, J.M. and Scheiner, S.M.: Plant diversity, biogeography and environment in Iberia:
847   Patterns and possible causal factors. J Veg Sci, 13, 245-258, 2002.

848   Rodó, X., Baert, E., Comin, F.A.: Variations in seasonal rainfall in Southern Europe during the
849   present century: relationships with the North Atlantic Oscillation and the El Niño-Southern
850   Oscillation. Clim Dynam, 13, 275-284, 1997.

851   Rodrigues et al.: The last glacial-interglacial transition (LGIT) in the western mid-latitudes of the
852   North Atlantic: Abrupt sea surface temperature change and sea level implications.
853   Quaternary Sci Rev, 29, 1853-1862, 2010.

854   Roucoux, K.H., de Abreu, L., Shackleton, N.J., Tzedakis, P.C.: The response of NW Iberian
855   vegetation to North Atlantic climate oscillations during the last 65kyr, Quaternary Sci Rev,
856   24, 1637-1653, 2005.

857   Roucoux, K.H., Tzedakis, P.C., de Abreu, L., Shackleton, N.J.: Climate and vegetation changes
858   180,000 to 345,000 years ago recorded in a deep-sea core off Portugal. Earth Planet Sci Lett,
859   249, 307-325, 2006.

860 Rousseau, D.D., Kukla, G., McManus, J.: What is what in the ice and the ocean? Quaternary Sci
861   Rev, 25, 2025-2030, 2006.

862 K. L. Rosanski, Araguas-Araguas, R. Gonfiantini, in *Climate Change in Continental Isotopic*
863   *Records*, P. K. Swart, K. C. Lohmann, J. McKenzie, S. Savin, Eds. (American Geophysical
864   Union, Washington, DC), pp. 1–36, 1993.

865 Saltzman, Matthew & Thomas, E. (2012). Carbon Isotope Stratigraphy. The Geologic Time
866   Scale, 1, 207-232. 2012.

867 Sánchez Goñi, M.F., Turon, J.L., Eynaud, F., Gendreau, S., European climatic response to
868   millennial-scale changes in the atmosphere-ocean system during the Last Glacial Period.
869   Quaternary Res, 54, 394-403, 2000.

870 Sánchez Goñi, M.F., Cacho, I., Turon, J-L., Guiot, J., Sierro, F.J., Peypouquet, J.-P., Grimalt,
871   J.O., Shackleton, N.J.: Synchroneity between marine and terrestrial responses to millennial
872   scale climatic variability during the last glacial period in the Mediterranean region. Clim
873   Dynam, 19, 95-105, 2002.

874 Sánchez Goñi, M.F., Landais, A., Fletcher, W.J., Naughton, F., Desprat, S., Duprat, J.:
875   Contrasting impacts of Dansgaard-Oeschger events over a western European latitudinal
876   transect modulated by orbital precession. Quaternary Sci Rev, 27, 1136-1151, 2008.

877 Sánchez Goñi, M.F., Bard, E., Landais, A., Rossignol, L., d'Errico, F.: Air-sea temperature
878   decoupling in western Europe during the last interglacial-glacial transition. Nat Geosci, 6,
879   837-841, 2013.

880 Sánchez Goñi, M.F., Rodrigues, T., Hodell, D.A., Polanco-Martinez, J.M., Alonso-Garcia, M.,
881   Hernandez-Almeida, I., Desprat, S., Ferretti, P.: Tropically-driven climate shifts in
882   southwestern Europe during MIS 19, a low eccentricity interglacial. Geophys Res Abst, 18,
883   EGU2016-3940, 2016.

884 Schneider, U., Becker, A., Finger, P., Meyer-Christoffer, A., Ziese, M., Rudolf, B.: GPCC's new
885   land surface precipitation climatology based on quality-controlled in situ data and its role in
886   quantifying the global water cycle. Theoret Appl Climatol, 115, 15-40, 2013.

887 Schneider, U., A. Becker, P. Finger, A. Meyer-Christoffer, M. Ziese, and B. Rudolf (2014),
888   GPCC's new land surface precipitation climatology based on quality-controlled in situ data
889   and its role in quantifying the global water cycle, Theor. Appl. Climatol., 115, 1–15.

890 Schrag, D.P, Hampt, G., and Murray, D.W.: Pore fluid constraints on the temperature and
891   oxygen isotopic composition of the glacial ocean. Science, 272, 5270, 1930-1932, 1996.

892 Spötl, C., Mangini, A., Richards, D.A.: Chronology and paleoenvironment of Marine Isotope
893   Stage 3 from two high-elevation speleothems, Austrian Alps. Quaternary Sci Rev, 25, 1127-
894   1136, 2006.

895 Stoll, H.M., Moreno, A., Mendez-Vincente, A., Gonzalez-Lemos, S., Jimenez-Sánchez, M.,
896   Dominguez-Cuesta, M.J., Edwards, R.L., Cheng, H., Wang, X.: Paleoclimate and growth
897   rates of speleothems in the northwestern Iberian Peninsula over the last two glacial cycles.
898   Quaternary Res, 80, 284-290, 2013.

899 Thatcher, D.L., Wanamaker, A.D., Jr., Denniston, R.F., Asmerom, Y., Ummenhofer, C.C.,
900   Polyak, V.J., Hasiuk, F., Haws, J.A., and Gillikin, D.P.: Changes in hydroclimate in Iberia in
901   the last 1200 years: insights from speleothem records from western Portugal. Geological
902   Society of America North-Central Meeting Abstracts with Programs, Ames, Iowa, 2018.

903 Trigo, R.M., Osborn, T.J., Corte-Real, J.M.: The North Atlantic Oscillation influence on Europe:
904   climate impacts and associated physical mechanisms, Clim Res, 20, 9-17, 2002.

905 Trouet, V., Esper, J., Graham, N.E., Baker, A., Scourse, J.D., Grank, D.C.: Persistent positive
906   North Atlantic Oscillation mode dominated the Medieval Climate Anomaly. Science, 324,
907   78-80, 2009.

908 Tzedakis, P.C., Roucoux, K.H., de Abreu, L., Shackleton, N.J.: The duration of forest stages in
909   southern Europe and interglacial climate variability, Science, 306, 2231-2235, 2004.

910 Vaks, A., Gutareva, O.S., Breitenbach, S.F.M., Avirmed, E., Mason, A.J., Thomas, A.L., Osinev,
911   A.V., Kononov, A.M., Henderson, G.M.: Speleothems reveal 500,000-year history of
912   Siberian permafrost. Science, 340, 183-186, 2013.

913 Vandenberghe, J., French, H.M., Gorbunov, A., Marchenko, S., Velichko, A.A., Jin, H., Cui,
914   Z., Zhang, T.,Wan, X.: The Last Permafrost Maximum (LPM) map of the Northern
915   Hemisphere: permafrost extent and mean annual air temperatures, 25-17 ka BP, Boreas, 43,
916   652–666, 2014.

917 Vegas, J., Ruiz-Zapata, B., Ortiz, J.E., Galan, L., Torres, T., Garcia-Cortes, A., Gil-Garcia, M.J.,
918   Perez-Gonzalez, A., Gallardo-Millan, J.L.: Identification of arid phases during the last 50 cal.
919   ka BP from the Fuentillejo maar-lacustrine record (Campo de Calatrava Volcanic Field,
920   Spain), J Quaternary Sci, 25, 1051-1062, 2010.

921   Voelker, A.H. L., Rodrigues, T., Stein, R., Hefter, J., Billups, K., Oppo, D., McManus, J,,

922   Grimalt, J.O.: Variations in mid-latitude North Atlantic surface water properties during the

923   mid-Brunhes (MIS 9-14) and their implications for thermohaline circulation, Clim Past, 6, p.

924   531-552, 2010.

925   Voelker, A.H.L. and de Abreu, L.: A review of abrupt climate change events in the northeastern

926   Atlantic Ocean (Iberian Margin): Latitudinal, Longitudinal, and Vertical Gradients. Abrupt

927   Climate Change: Mechanisms, Patterns, and Impacts (Eds. Rashid, H., Polyak, L., and

928   Mosley-Thompson, E.), Geophysical Monograph Series 193, 15-37, 2011.

929   Wainer, K., Genty, D., Blamart, D., Daëron, M., Bar-Matthews, M., Vonhof, H., Dublyansky,

930   Y., Pons-Branchu, E., Thomas, L., van Calsteren, P., Quinif, Y., and Caillon, N.: Speleothem

931   record of the last 180 ka in Villars cave (SW France): Investigation of a large $\delta^{18}O$ shift

932   between MIS6 and MIS5. Quaternary Sci. Rev., 30, 130-146, 2011.

933   Zhou, J., Lundstrom, C.C., Fouke, B., Panno, S., Hackley, K., and Curry, B. Geochemistry of

934   speleothem records from southern Illinois: Development of $(^{234}U)/(^{238}U)$ as a proxy for

935   paleoprecipitation. Chemical Geology, 221, 1-20, 2005.

936

937

938
939
940
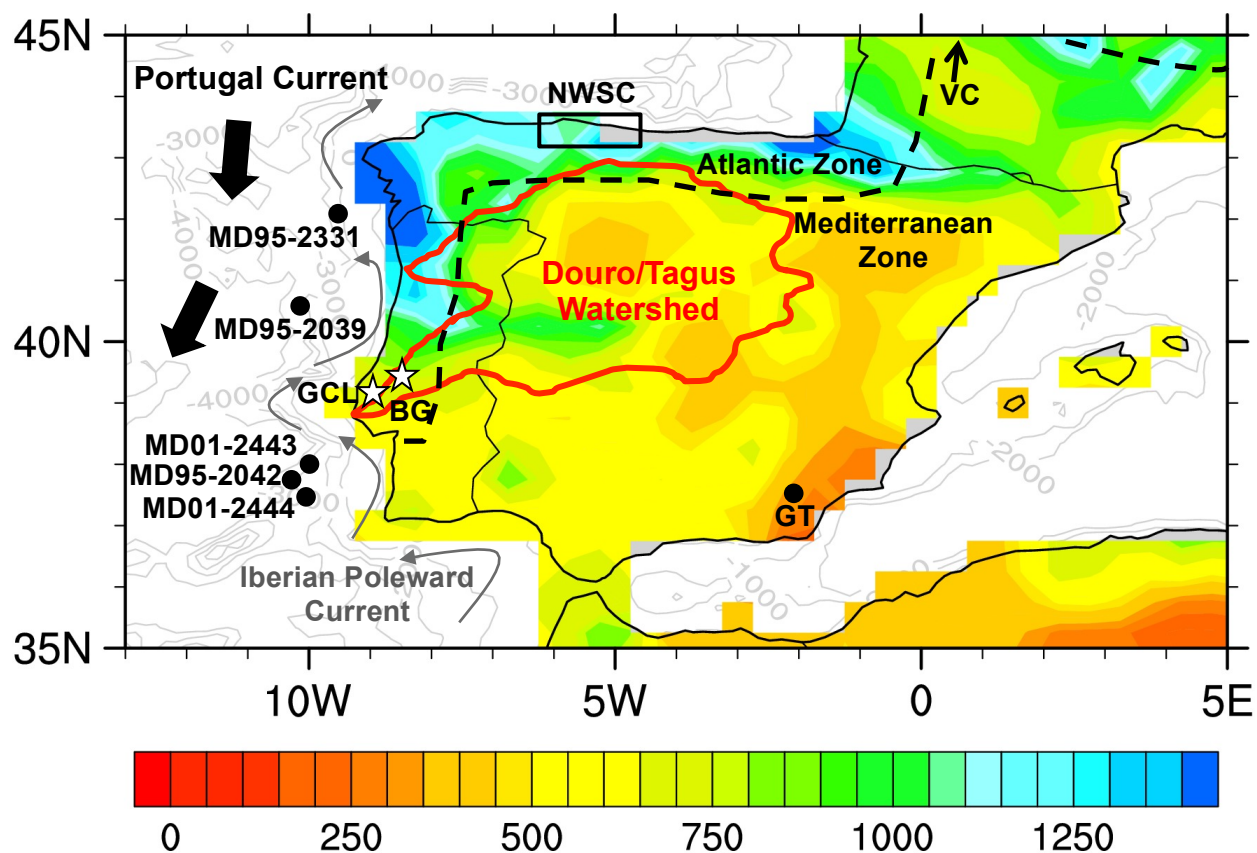
Figure 1. Average annual precipitation (mm) of the Iberian Peninsula for years AD 1901-2009 (GPCC v. 6; Schneider et al., 2013) relative to cave study sites (white stars: GLC = Gruta do Casal da Lebre; BG = Buraca Gloriosa). Rectangle denotes location of northwest Spain cave sites (NWSC) (Moreno et al., 2010; Stoll et al., 2013); FM = Fuentillejo maar (Vegas et al., 2010) and GT = Gitana cave (Hodge et al., 2008); VC = Villars Cave (Genty et al., 2003) located just north of map. Also shown are locations of marine cores discussed in text and GNIP station at Porto. Bathymetric contours shown in grey (m). Location of currents after Voelker et al. (2010).

949
950

951

952

953
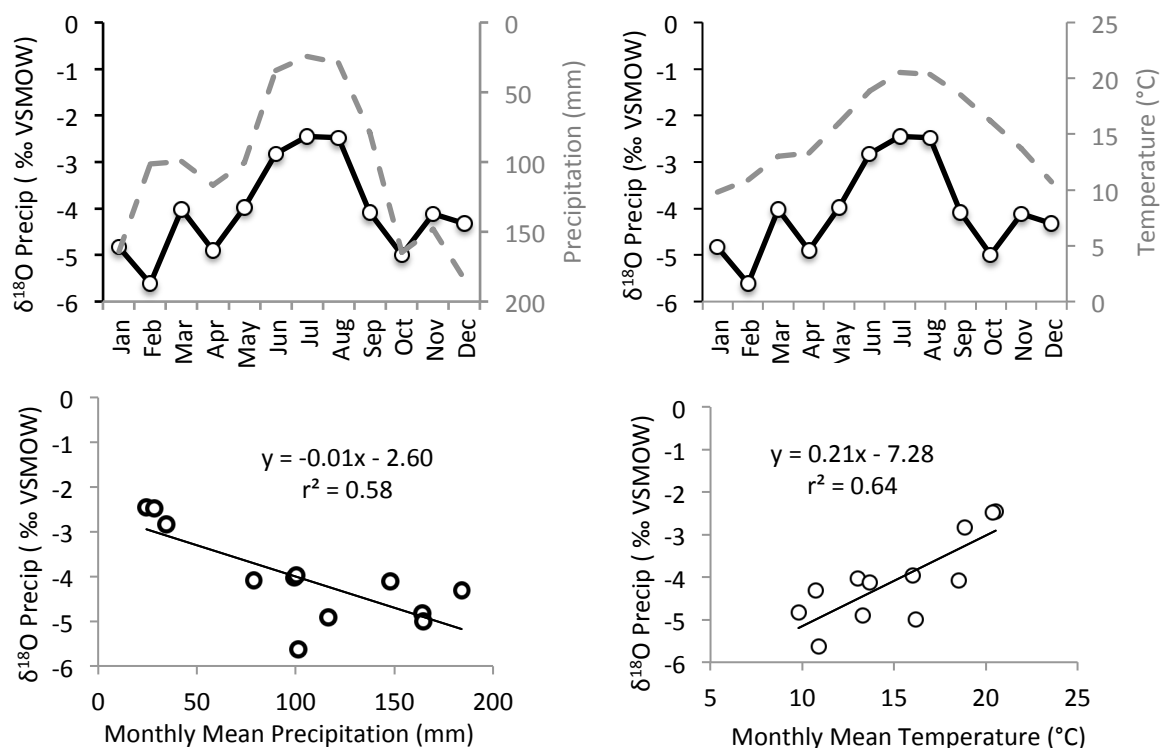
Figure 2. Oxygen isotopic composition of precipitation versus rainfall amount (lefthand panels) and air temperature (righthand panels). Data collected at IAEA/GNIP site in Porto, Portugal (see Fig. 1 for location) for 1988-2004. Oxygen isotope data represent multi-year averages of monthly means. Note that righthand y-axis in upper left panel is inverted in order to illustrate inverse nature of rainfall and precipitation oxygen isotopic composition.

959

960
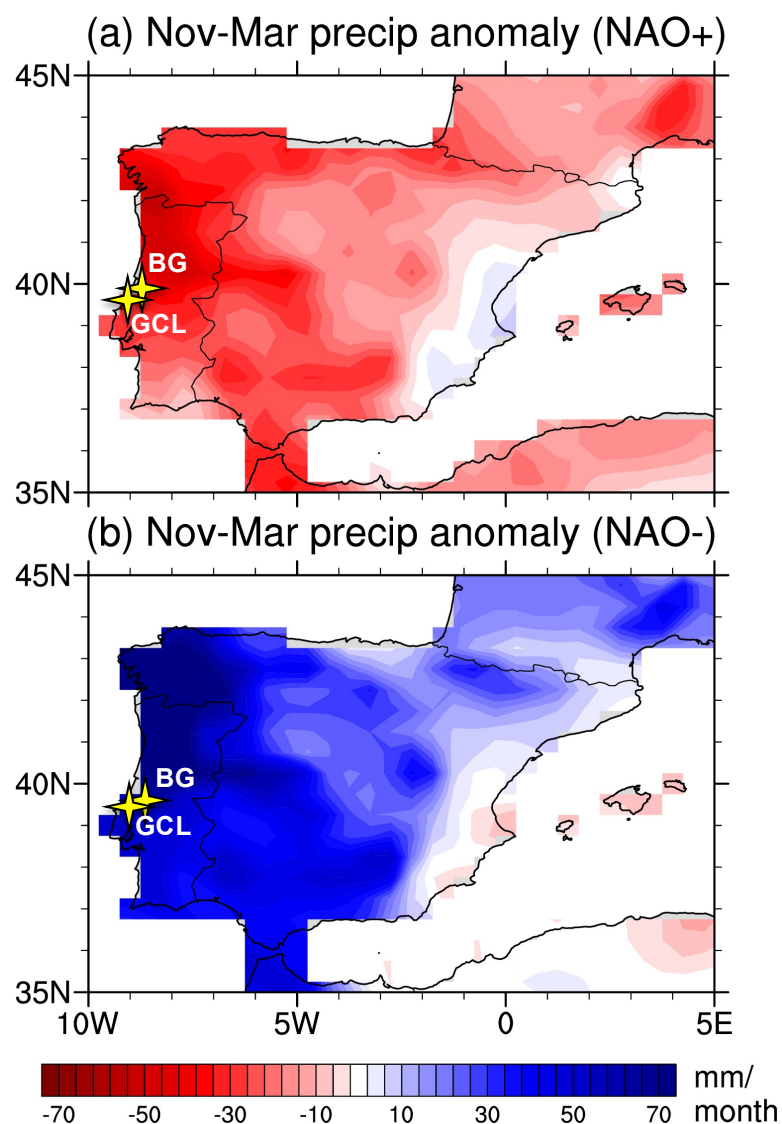
Figure 3. Iberian rainfall anomalies associated with the North Atlantic Oscillation. Composites of November-March precipitation anomalies (mm/month) during (a) positive and (b) negative NAO winters for the period 1901-2012. Positive/negative NAO winters were determined using the December-March Hurrell principal component-based NAO index (CDG, 2018) as those winters with NAO values in the highest/lowest decile of all winters. The PC-based NAO index represents the time series of the leading Empirical Orthogonal Function of SLP anomalies over the Atlantic sector, 20°-80°N, 90°W-40°E. Precipitation anomalies are based on the GPCC precipitation, version 7, at 0.5˚ spatial resolution (Schneider et al. 2014). Yellow stars denote cave sites in this study: BG = Buraca Gloriosa; GCL = Gruta do Casal da Lebre.
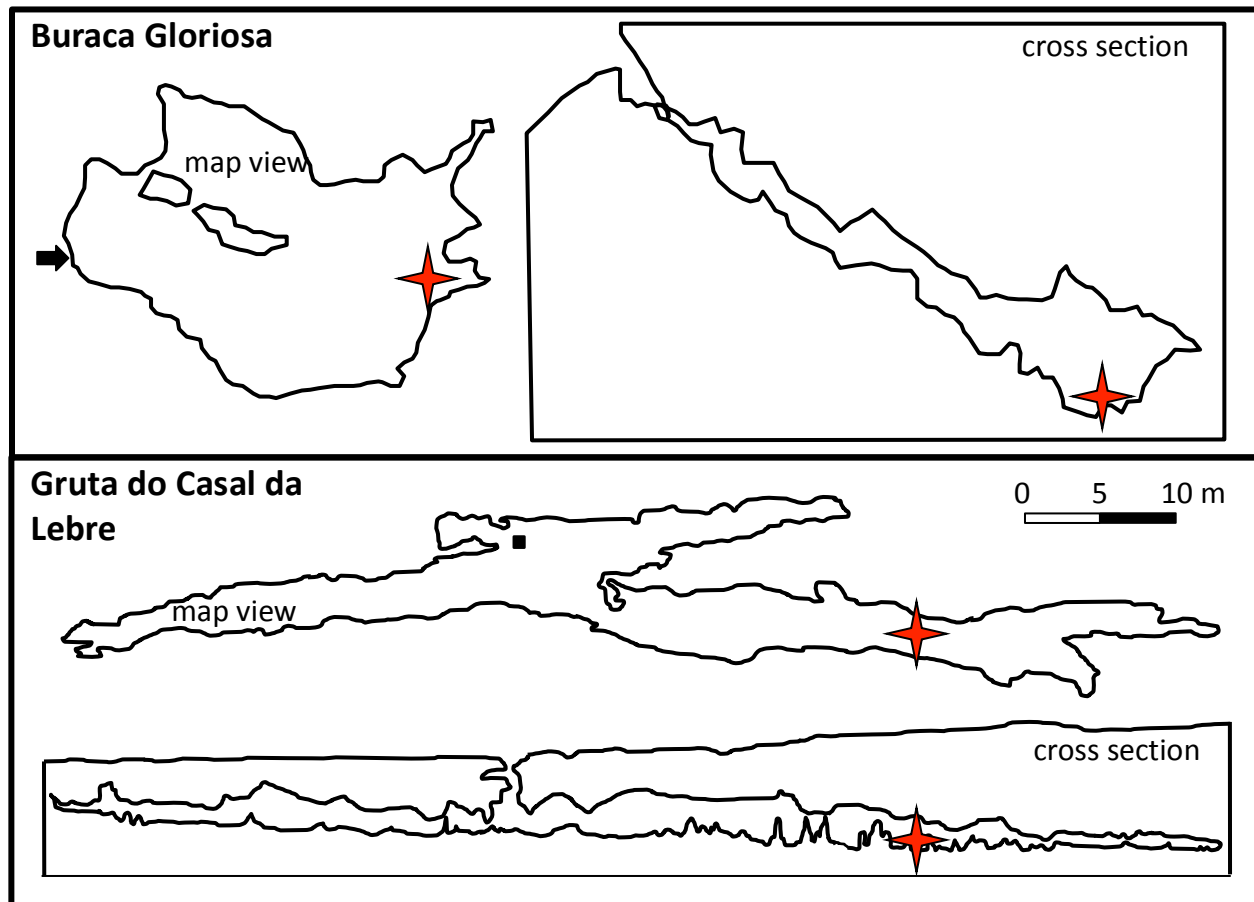
Figure 4. Profile and map views of Buraca Gloriosa (top) and Gruta do Casal da Lebre (bottom). Entrance denoted by arrow (top panel) and filled square (bottom panel). Red stars denote locations of stalagmites used in this study.
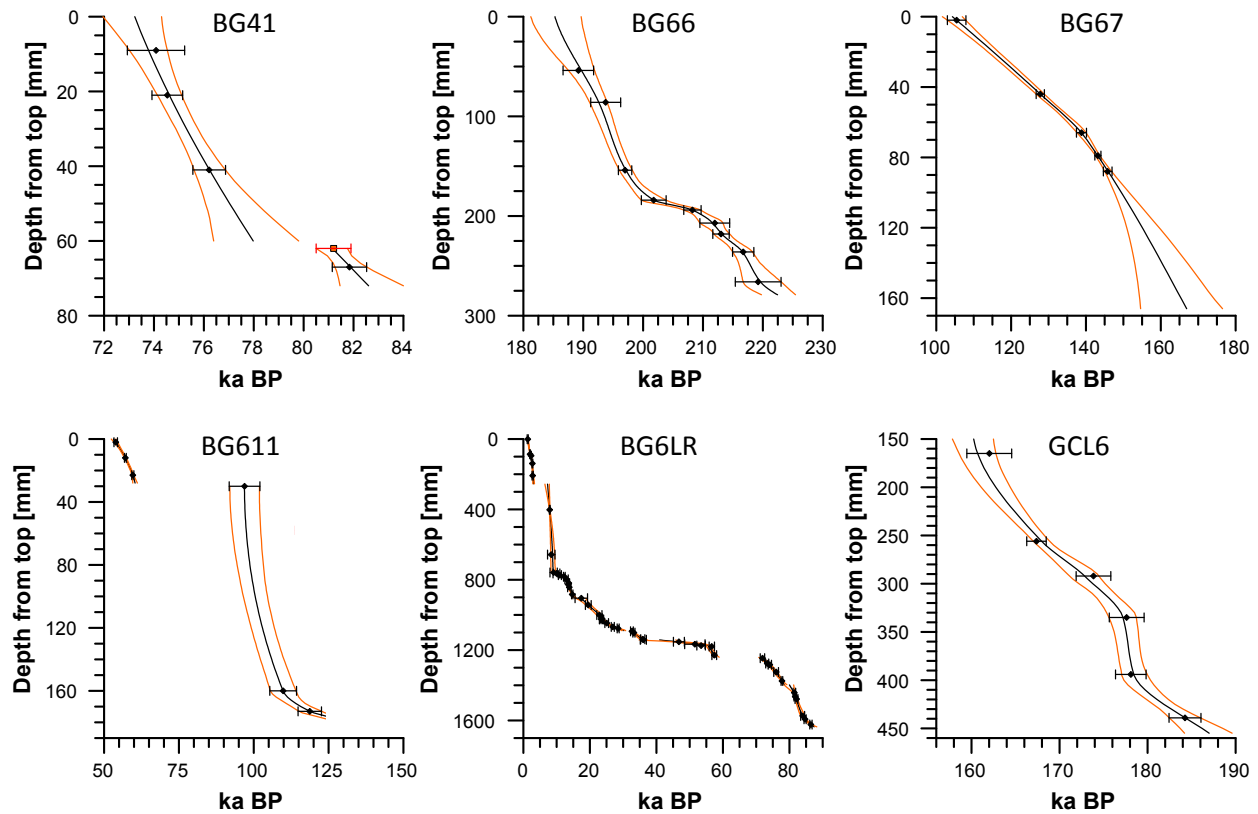
Figure 5. COPRA-derived age models for BG/GCL stalagmites. Black lines represent mean of calculated age models while red lines denote 95% confidence intervals. See Table 1 for specific ages and isotopic ratios. Orange square represents a "dummy age" that was included in order to extrapolate below the hiatus, which is only possible with at least two dated points. The bottom of BG611 was based on linear extrapolation through dated intervals.
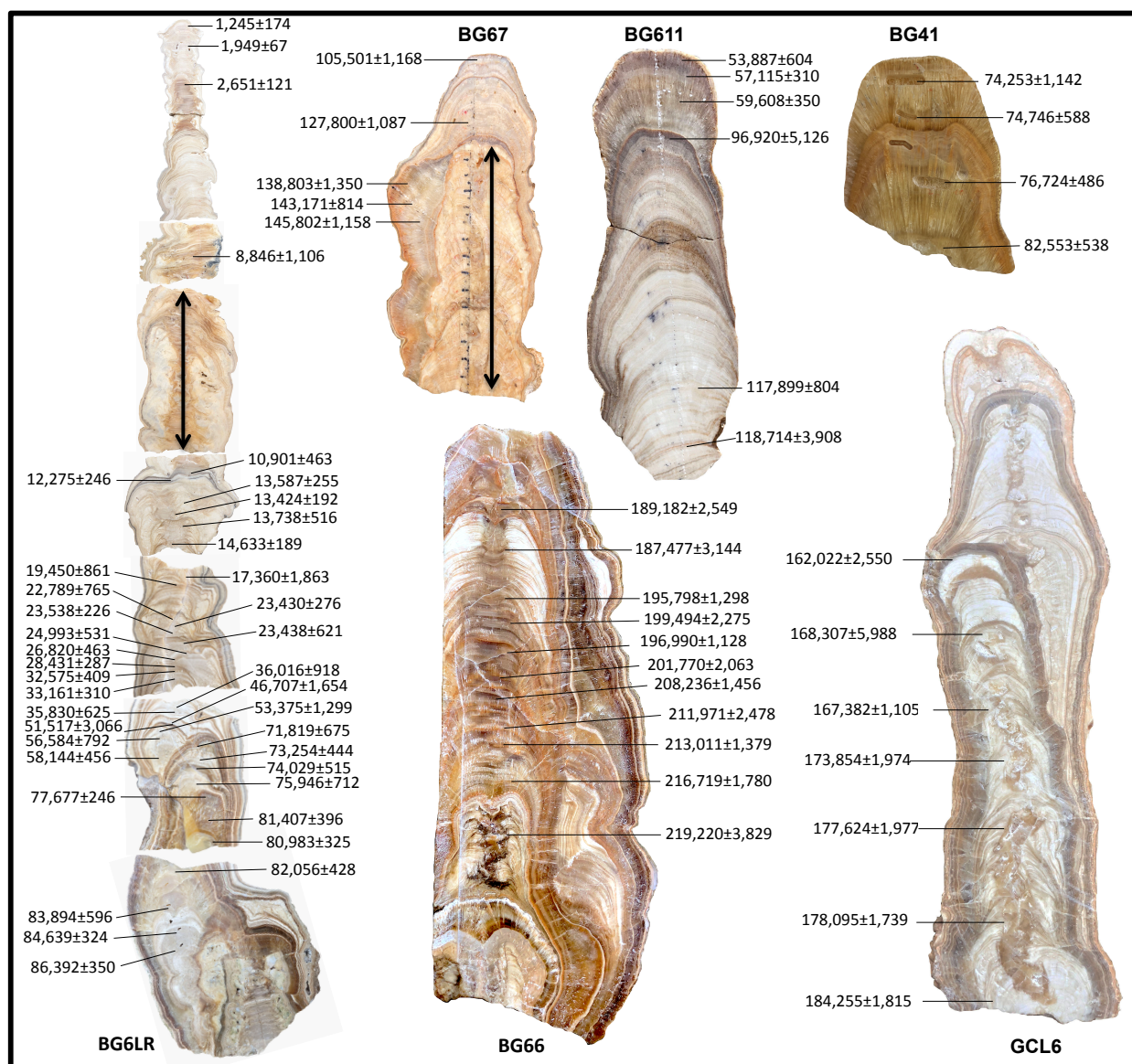
987
988
989 **Figure 6. BG/GCL stalagmites and U/Th ages.** Black arrows represent intervals excluded from
990 this study due to evidence of open system behavior.
991
992
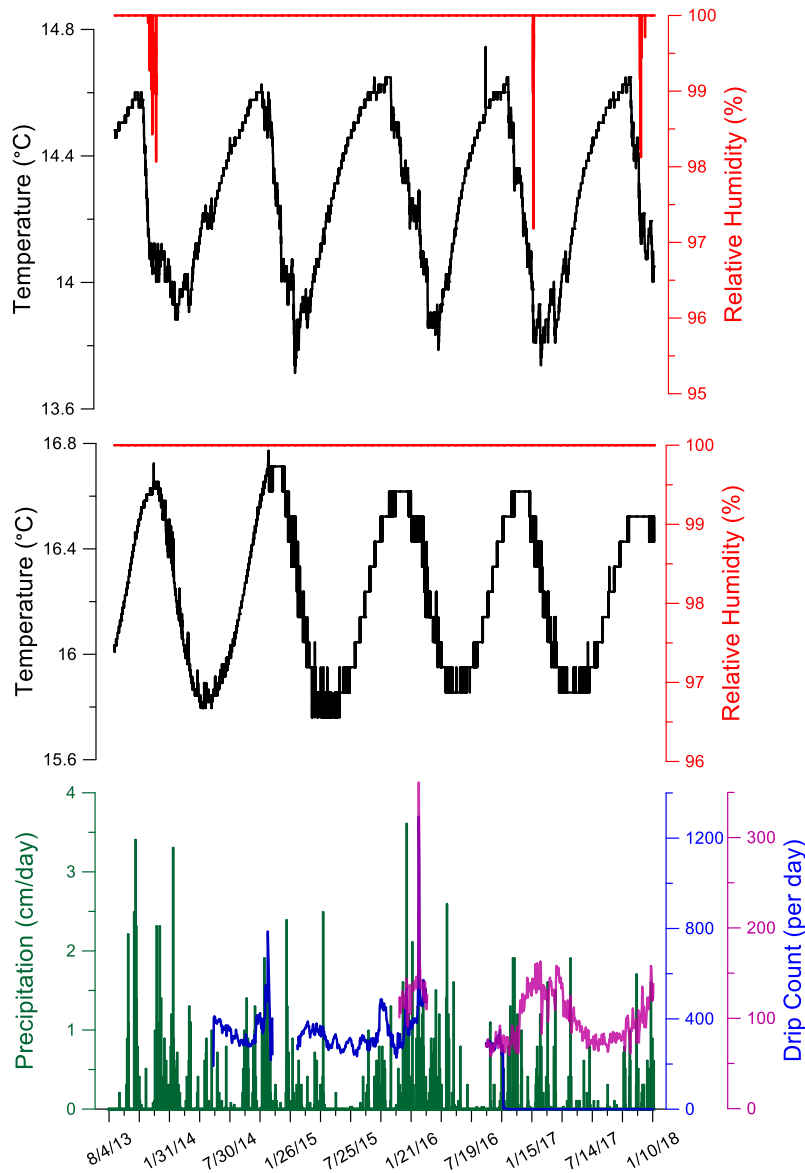
Figure 7. Temperature and relative humidity variations from (top) Buraca Gloriosa and (middle) GCL. Drip rate from Buraca Gloriosa and precipitation variability (bottom) from Monte Real, Portugal (35 km from BG). Temperature sensor in GCL was changed in November 2014 and the sensitivity of the new instrument varies slightly from the original.
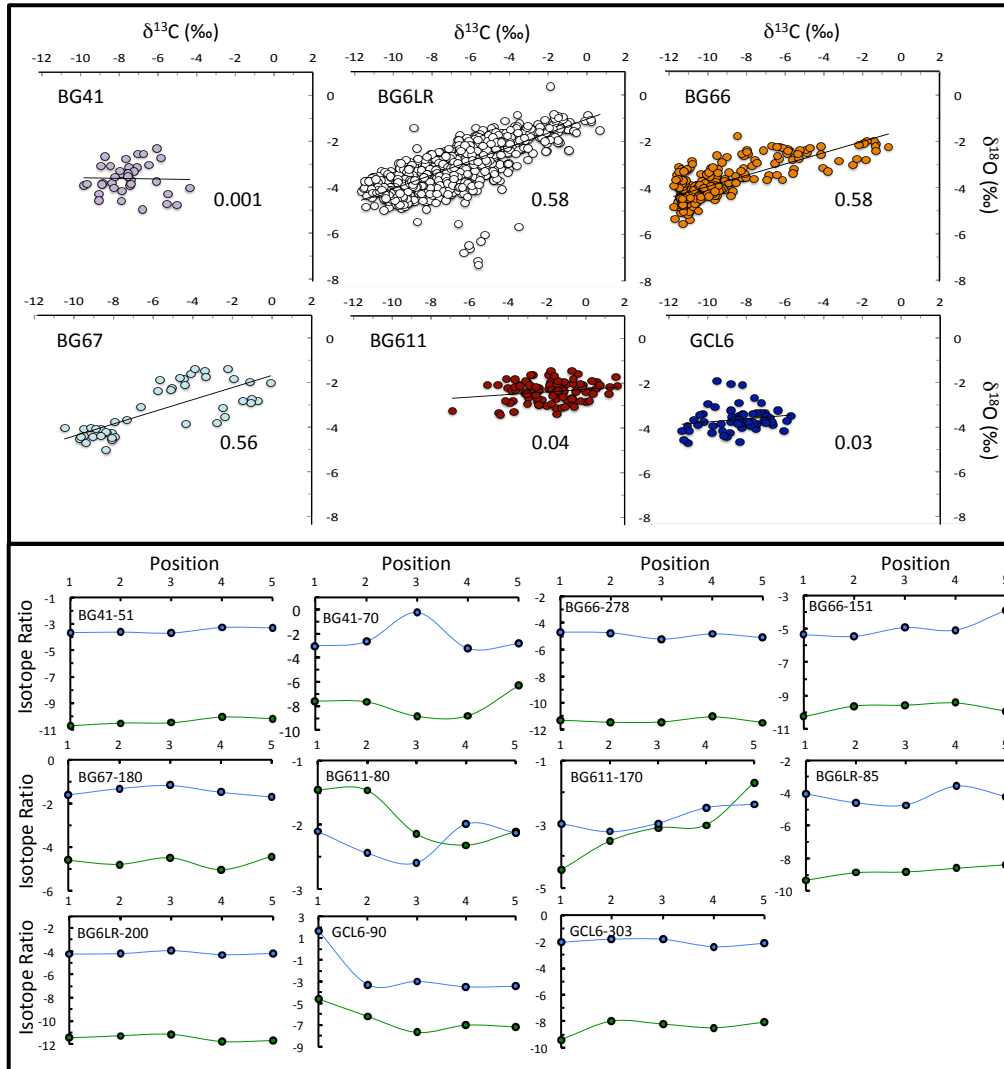
1000
1001
1002 **Figure 8.** Hendy Tests of BG/GCL stalagmites. Top: Covariance plots of carbon and oxygen
1003 isotopic ratios. Correlation coefficients (r^2 values) are listed for each plot. High positive
1004 correlations have been identified as an indicator of non-equilibrium crystallization. Bottom:
1005 Oxygen (blue) and carbon (green) isotopic variations along the same growth layers with distance
1006 (listed in the upper left corner of each panel) from the stalagmite central growth axis. Progressive
1007 increases in $d^{18}O$ values have been interpreted to reflect disequilibrium crystallization.
1008 Limitations of the Hendy Tests are discussed in text.
1009
1010
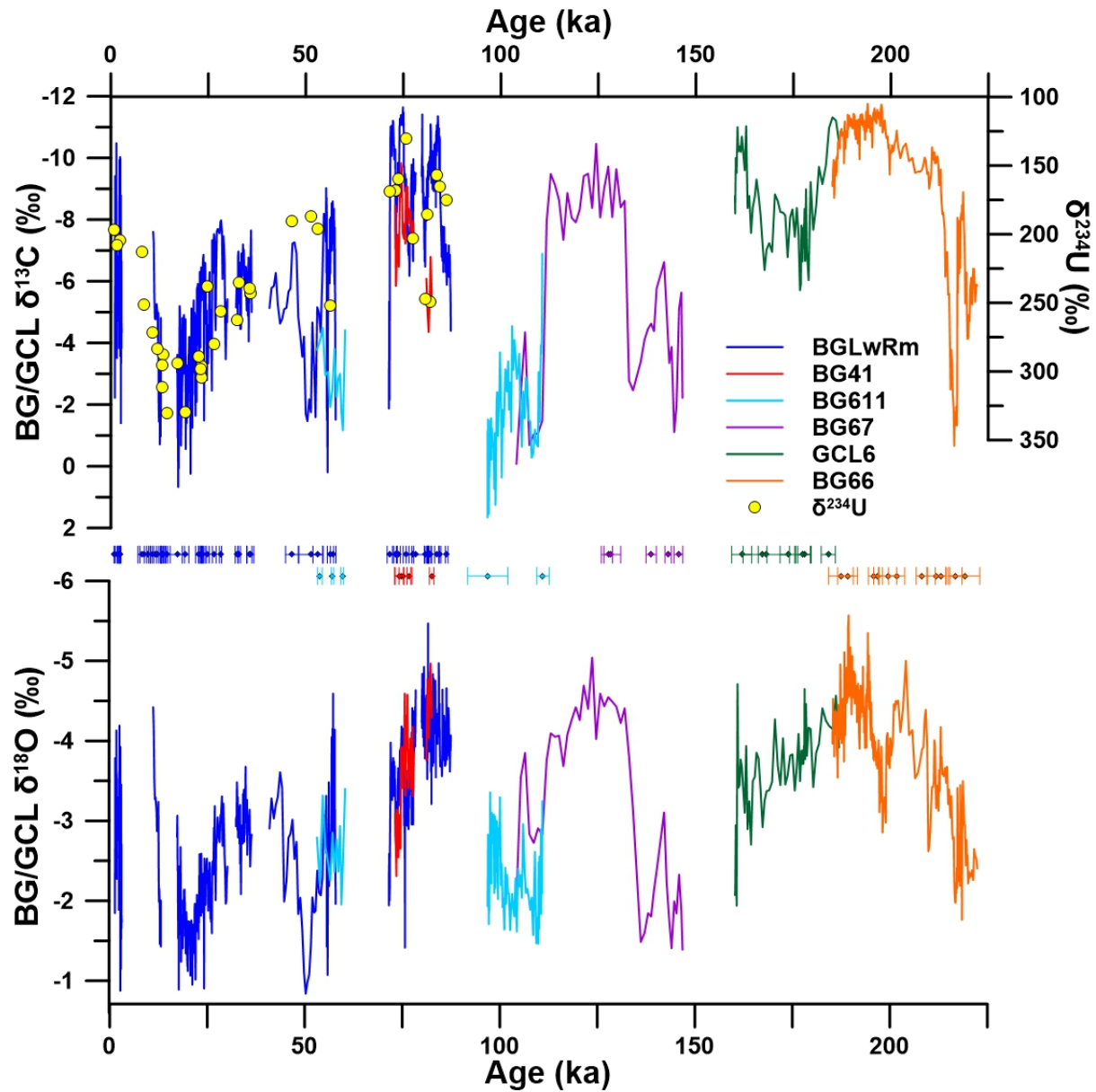
1011
1012
1013 **Figure 9. BG/GCL stalagmite isotopic time series**. Carbon (top) and oxygen (bottom) isotopes,
1014 with each stalagmite presented in a different color. $d^{234}U$ values (yellow circles) for BG6LR are
1015 plotted against carbon isotope ratios (plots showing the $d^{234}U$ and $d^{13}C$ values of the other
1016 stalagmites are presented in the Supplemental Material). U/Th ages (with 2 s.d. errors) are also
1017 shown.
1018
1019
1020
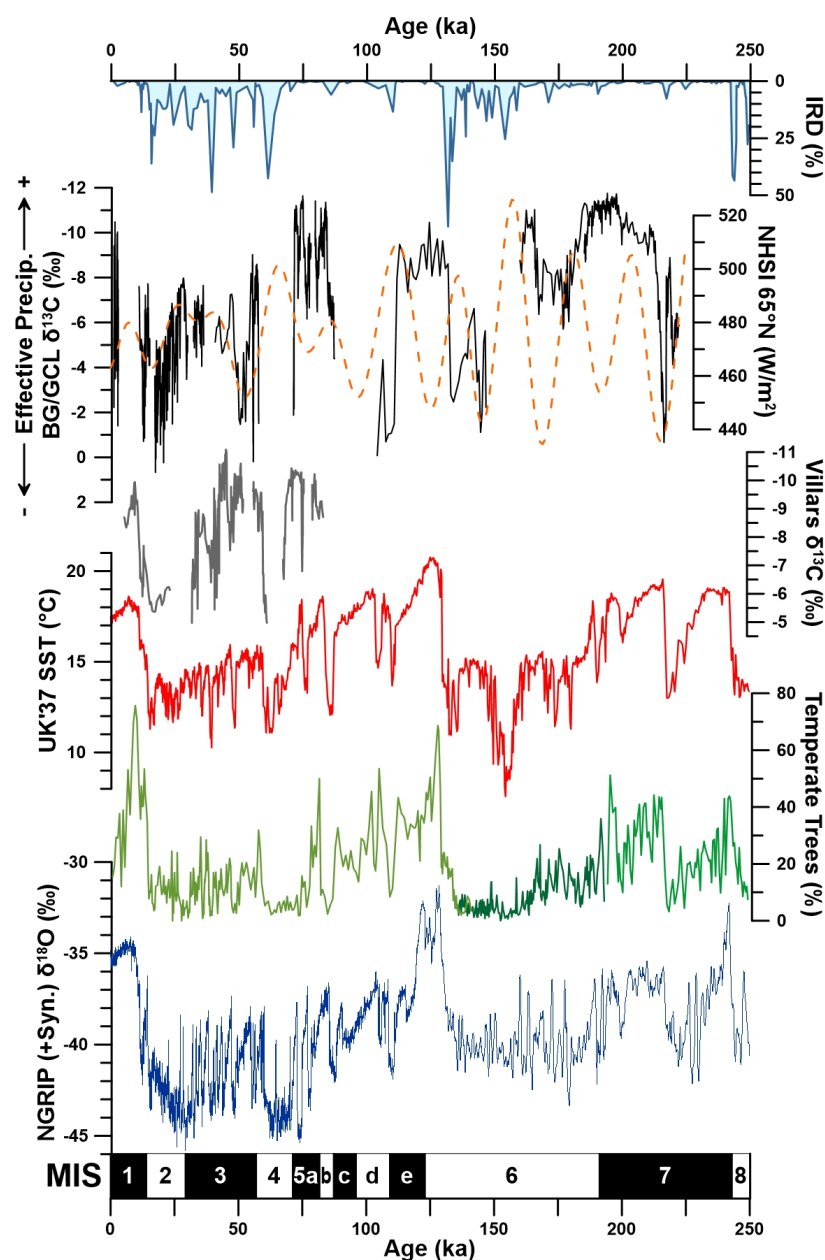
1021
1022
1023 **Figure 10. Comparison of Portuguese stalagmite hydroclimate proxies with regional and**
1024 **global climate records from the last two glacial cycles** (A) Ice-rafted debris abundance from
1025 North Atlantic ODP Site 980 (McManus et al., 1999 using Hulu cave time scale as presented in
1026 Barker et al., 2011); (B) composite BG/GCL stalagmite carbon isotopic time series with NH
1027 summer insolation (Berger an Loutre, 1991); (C) Carbon isotopic time series from Villars Cave,
1028 southern France (Genty et al., 2003; Genty et al., 2006); (D) Alkenone-based Iberian margin SST
1029 reconstruction (core MD01-2443; Martrat et al., 2007); (E) Temperate forest pollen abundance
1030 from three closely spaced cores (MD01-2443: 250-194 ka (Roucoux et al, 2006; Tzedakis et al.,
1031 2004); MD01-2444: 194-136 ka (Margari et al., 2010; Margari et al., 2014); MD95-2042: 136-1
1032 ka (Sánchez Goñi et al., 2008; Sánchez Goñi et al., 2013)); (F) NGRIP (0-122 ka) (North
1033 Greenland Ice Core Project members, 2004) and synthetic Greenland oxygen isotopic record
1034 (Barker et al., 2011) and (G) marine isotope stages.
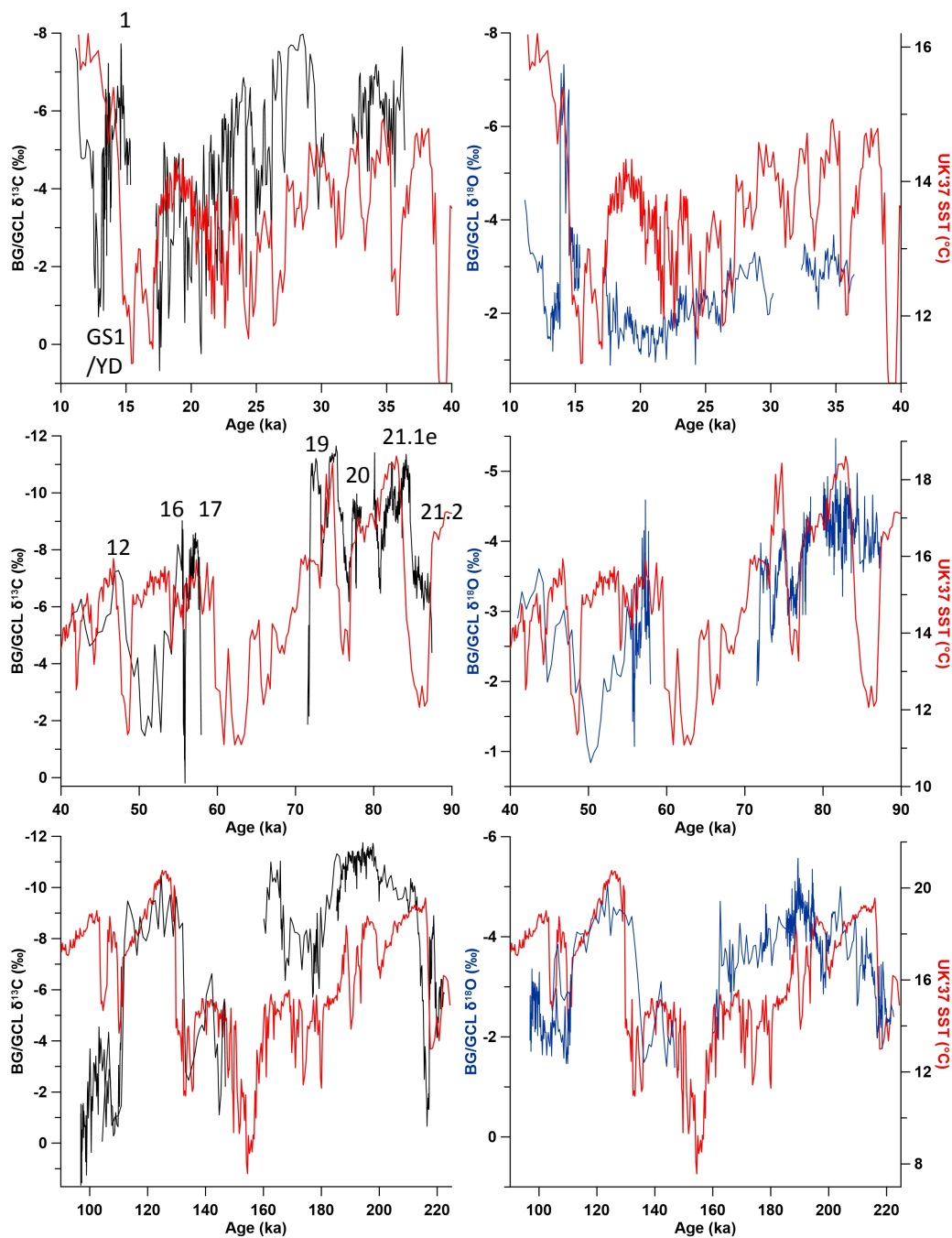
1035
1036
1037 **Figure 11. Iberian margin SST (red) and stalagmite carbon (black) and oxygen (blue)**
1038 **isotopes.** Numbers denote select GI events using stratigraphic nomenclature of Rasmussen et al.
1039 (2014).
1040
1041
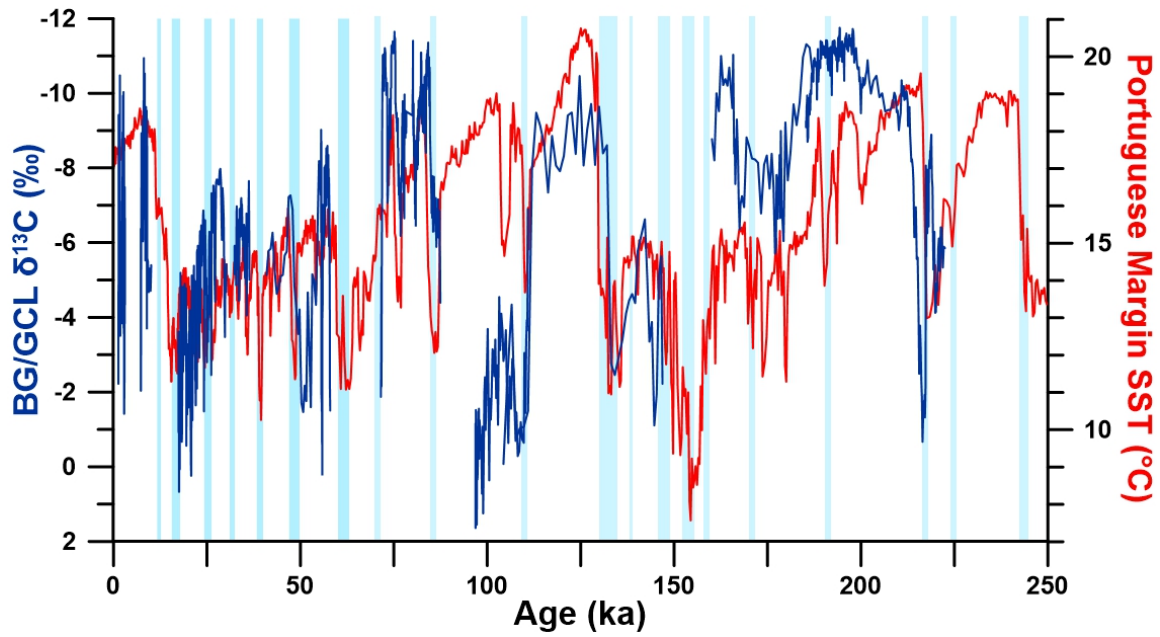
Figure 12. BG/GCL stalagmite carbon isotopic time series and Iberian margin SST. Light blue vertical rectangles denote North Atlantic cold events (some of which are labeled). Several interruptions in stalagmite growth coincide, within the errors of the stalagmite chronologies, with periods of depressed SST.

0Table 1. U/Th Isotopic Ratios and ²³⁰Th Ages

Stalagmite	Distance to Top (mm)[a]	²³⁸U (ng/g)	²³²Th (pg/g)	δ²³⁴U[b] (corr'd)	Error[c]	²³⁰Th/²³⁸U (activity)	Error	²³⁰Th/²³²Th (ppm)	Error	Uncorrected Age (yr BP)[d]	Error (yr)	Corrected Age (yr BP)[e]	Error (yr)
BG41	67	148	2,892	524.7	2.2	0.779	0.0023	657.7	18.6	82,926	389	82,553	538
BG41	41	293	4,635	522.8	2.2	0.742	0.0030	773.8	8.5	77,026	463	76,724	486
BG41	21	217	1,858	566.6	3.1	0.748	0.0039	1,440.0	40.6	74,906	567	74,746	588
BG41	9	271	2,088	610.8	9.8	0.764	0.0073	1,635.6	22.3	74,392	1,135	74,253	1,142
BG66	266	85	6,980	698.6	9.3	1.283	0.0057	256.5	1.8	223,637	3,252	219,220	3,829
BG66	236	123	4,742	520.6	4.1	1.169	0.0030	500.0	4.0	217,460	1,752	216,719	1,780
BG66	218	101	3,132	532.4	3.1	1.174	0.0015	623.6	4.6	214,835	1,052	213,011	1,379
BG66	207	75	4,657	429.2	3.8	1.116	0.0025	298.1	1.7	215,891	1,580	211,971	2,478
BG66	194	68	2,003	499.5	3.1	1.149	0.0019	644.2	7.4	210,002	1,175	208,236	1,456
BG66	184	95	4,336	379.4	3.1	1.073	0.0025	386.6	3.6	204,768	1,460	201,770	2,063
BG66	154	104	2,193	443.5	2.6	1.100	0.0015	864.2	11.9	198,297	930	196,990	1,128
BG66	120	82	1,476	293.1	3.9	1.015	0.0030	933.1	29.6	200,740	1,920	199,494	2,275
BG66	86	104	2,661	345.4	2.4	1.041	0.0016	672.5	8.4	197,507	994	195,798	1,298
BG66	73	91	6,080	389.7	5.1	1.061	0.0047	263.1	1.9	191,832	2,368	187,477	3,144
BG66	54	76	995	564.2	6.2	1.159	0.0057	1,453.3	64.3	189,936	2,538	189,182	2,549
BG67	88	320	2,153	617.8	2.9	1.095	0.0043	2,689.7	51.5	146,174	1,146	145,802	1,158
BG67	79	195	2,799	485.8	2.3	1.014	0.0022	1,164.3	18.2	144,037	695	143,171	814
BG67	66	250	4,187	610.3	4.9	1.072	0.0046	1,057.4	12.7	139,735	1,279	138,803	1,350
BG67	44	162	4,858	484.7	2.4	0.969	0.0023	531.9	5.3	129,620	608	127,800	1,087
BG67	2	216	5,542	401.5	2.6	0.837	0.0039	538.0	5.1	107,150	843	105,501	1,168
BG611	173	119	11,744	202.6	3.5	0.801	0.0041	133.9	0.8	126,291	1,253	118,714	3,908
BG611	112	99	3,304	238.0	3.0	0.776	0.0038	383.6	5.6	113,518	1,028	111,086	1,574
BG611	30	122	16,801	251.3	5.0	0.762	0.0043	91.2	0.5	107,202	1,088	96,920	5,126
BG611	23	313	552	340.8	1.4	0.553	0.0024	5,168.2	353.7	59,726	345	59,608	350
BG611	12	248	2,233	356.2	1.6	0.547	0.0021	1,002.4	25.4	57,908	296	57,115	310
BG611	2	250	4,109	376.7	1.8	0.533	0.0021	535.0	5.9	54,959	284	53,887	604
BG6LR	1,623	72	133	175.0	1.5	0.631	0.0015	5,665.9	1,162	86,532	342	86,392	350
BG6LR	1,593	98	140	165.3	1.4	0.618	0.0014	7,166.0	1,764	84,748	318	84,639	324
BG6LR	1,574	74	905	156.6	1.6	0.615	0.0016	824.8	25.3	84,848	360	83,894	596
BG6LR	1478	159	26	249.2	1.8	0.645	0.0021	63,745.2	114,070	82,068	428	82,056	428
BG6LR	1464	166	1,138	246.8	1.5	0.641	0.0009	1,542.3	35.8	81,475	214	80,983	325
BG6LR	1442	162	77	185.4	1.4	0.634	0.6339	21,885.5	13,015	81,442	396	81,407	396
BG6LR	1375	112	220	202.9	1.5	0.602	0.6016	5,064.2	652.0	77,823	234	77,677	246
BG6LR	1324	120	1,908	130.2	1.4	0.566	0.5660	585.8	15.3	77,213	330	75,946	712
BG6LR	1283	132	1,019	159.5	2.0	0.566	0.5659	1,213.9	71.1	74,623	422	74,029	515
BG6LR	1276	105	353	167.8	2.1	0.564	0.5637	2,766.4	298.1	73,512	425	73,254	444
BG6LR	1246	83	1,232	168.7	1.4	0.561	0.5613	625.8	14.2	72,957	369	71,819	675
BG6LR	1179	62	1,114	252.0	2.6	0.507	0.5071	464.4	15.9	57,877	465	56,584	792
BG6LR	1174	77	2,544	196.0	2.2	0.474	0.4736	235.4	3.8	55,882	375	53,375	1,299
BG6LR	1166	5	367	187.1	2.6	0.482	0.4821	100.4	1.6	57,644	524	51,517	3,066
BG6LR	1153	81	3,460	190.7	2.2	0.433	0.4331	167.2	2.3	49,960	367	46,707	1,654
BG6LR	1141	52	1,159	242.6	2.8	0.359	0.3591	266.4	10.4	37,626	449	36,016	918
BG6LR	1138	55	750	239.5	1.8	0.352	0.3518	426.3	33.1	36,815	381	35,830	625
BG6LR	1101	71	283	235.2	2.0	0.323	0.3234	1,344.2	198.7	33,449	272	33,161	310
BG6LR	1093	70	472	262.1	2.1	0.327	0.3269	802.0	73.4	33,052	331	32,575	409
BG6LR	1077	101	595	256.6	1.8	0.290	0.2899	810.6	63.4	28,851	193	28,431	287
BG6LR	1068	85	1,034	280.0	1.4	0.285	0.2847	384.9	15.5	27,675	178	26,820	463
BG6LR	1046	56	705	238.2	2.2	0.260	0.2603	339.0	19.7	25,911	265	24,993	531
BG6LR	1026	123	2,093	304.1	1.9	0.262	0.2617	253.3	8.5	24,612	206	23,438	621
BG6LR	1025	123	493	296.4	1.4	0.253	0.0017	1,041.2	151.0	23,814	175	23,538	226
BG6LR	1019	80	377	298.5	2.1	0.252	0.2525	887.3	107.4	23,753	221	23,430	276
BG6LR	1001	68	1,464	288.7	1.5	0.256	0.2558	196.1	4.3	24,291	156	22,789	765
BG6LR	944	76	1,896	329.3	2.1	0.233	0.2330	154.8	3.9	21,131	196	19,450	861
BG6LR	899	79	4,209	294.0	3.4	0.227	0.2266	70.6	1.3	21,074	283	17,360	1,863
BG6LR	883	91	233	330.3	2.0	0.168	0.1684	1,082.0	213.7	14,806	165	14,633	189
BG6LR	843	100	1,409	287.7	4.0	0.162	0.1623	190.4	6.7	14,718	164	13,738	516
BG6LR	827	103	332	295.0	2.9	0.152	0.1521	783.5	116.9	13,645	154	13,424	192
BG6LR	819	75	491	311.6	1.4	0.158	0.1581	400.0	22.8	14,032	123	13,587	255
BG6LR	783	95	525	283.8	2.2	0.141	0.1406	418.7	35.3	12,661	150	12,275	246
BG6LR	774	107	1,351	271.4	1.4	0.130	0.1304	169.8	5.7	11,795	119	10,901	463
BG6LR	759	135	4,177	251.5	1.5	0.121	0.1210	64.7	1.0	11,071	117	8,846	1,113
BG6LR	657	86	2,566	212.9	1.4	0.112	0.1120	62.1	0.9	10,540	96	8,326	1,106
BG6LR	139	172	323	204.2	1.7	0.031	0.0010	272.6	41.0	2,790	96	2,651	121
BG6LR	86	155	80	207.9	1.7	0.022	0.0007	720.9	312.3	1,987	62	1,949	67
BG6LR	1	122	43	196.7	18.9	0.014	0.0019	677.5	519.3	1,271	173	1,245	174
GCL6	439	91	2,815	76.3	2.3	0.862	0.0029	461.2	9.3	185,093	1,779	184,255	1,815
GCL6	394	86	3,009	125.7	2.0	0.881	0.0032	415.9	6.9	179,002	1,692	178,095	1,739
GCL6	335	70	4,579	82.7	3.0	0.856	0.0029	214.9	2.3	179,406	1,794	177,624	1,977
GCL6	292	75	2,61	78.2	2.9	0.845	0.0035	481.0	9.0	174,639	1,949	173,854	1,974
GCL6	256	116	1,019	86.2	2.2	0.836	0.0020	1,574.3	71.8	167,617	1,102	167,382	1,105
GCL6	208	7	186	92.9	2.6	0.843	0.0124	522.0	99.0	169,018	6,007	168,307	5,988
GCL6	165	94	2,507	122.4	4.2	0.847	0.0049	526.3	13.4	162,712	2,368	162,022	2,550

[a] Distances are relative to the base of the stalagmite; negative distances reflect measurements on basal portions obtained in subsequent field seasons.
[b] δ²³⁴U$_{meas'd}$ = [(²³⁴U/²³⁸U)$_{meas'd}$/(²³⁴U/²³⁸U)$_{eq}$-1] x 10³, where (²³⁴U/²³⁸U)$_{eq}$ is secular equilibrium activity ratio: $\lambda_{238}/\lambda_{234}$ = 1.0. Values reported as permil.
[c] Errors are at the 2σ level.
[d] Present is defined as the year AD 1950.
[e] Initial ²³⁰Th/²³²Th atomic ratio of 13.5x10⁻⁶ ± 6.75x10⁻⁶ used to correct for unsupported ²³⁰Th. BG stalagmites use 4.4x10⁻⁶ ± 2.2x10⁻⁶.

1049